Weakly non linear modeling of submerged wave energy converters

Lucas Letournel, Camille Chauvigné, Baptiste Gelly, Aurélien Babarit, Guillaume Ducrozet, Pierre Ferrant

Weakly Non linear Modeling of Submerged Wave Energy Converters

LETOURNEL Lucas[a,*], CHAUVIGNE Camille[a,b], GELLY Baptiste[a], BABARIT Aurélien[a], DUCROZET Guillaume[a], FERRANT Pierre[a]

[a] *École Centrale de Nantes, LHEEA Lab., UMR6598, Nantes, France*
[b] *IFP-EN, Rueil-Malmaison, France*

Abstract

Wave-to-Wire numerical models being developed for the study of wave energy converters usually make use of linear potential flow theory [1, 2, 3, 4, 5] to describe wave-structure interaction. This theory is highly efficient from a computational perspective. However, it relies on assumptions of small wave steepness and small amplitude of motion around mean positions. Often, maximization of wave energy converters' energy performance implies large amplitude motion [6, 7, 8], thus contradicting the assumption of small amplitude motion.

An alternative approach is to linearize the free surface conditions on the instantaneous incident wave elevation (Weak-Scatterer approach [9]) while the body conditions are evaluated at the exact body position. Studies of wave energy converters' dynamic response using this method are expected to be more accurate, while maintaining a reasonable computational time. With this aim, a Weak-Scatterer code (CN_WSC) was developed and used to study two submerged wave energy converters. The first is a heaving submerged sphere and the second is a bottom-hinged fully submerged oscillating flap. They are inspired respectively by the Ceto [10] and WaveRoller [11] devices.

Initial calculations were performed in linear conditions first to verify the CN_WSC against linear theory. Subsequently, calculations in nonlinear conditions were performed, using large wave steepness and amplitude of body motion. In linear conditions, results of CN_WSC showed good agreement with linear theory, whereas significant deviations from linear theory were observed in nonlinear conditions. As amplitude of body motion increases, linear theory tends to overestimate energy performance in comparison with weak-scatterer theory. In contrast, with smaller amplitude of motion but larger wave steepness, the opposite result is obtained: energy performance is underestimated by linear theory compared to weak-scatterer theory.

Keywords: Wave Energy Converter, Numerical modeling, Potential Free-Surface Flow, Weak-Scatterer, Energy performance

*Corresponding author
Email address: lucas.letournel@ec-nantes.fr (LETOURNEL Lucas)

1. INTRODUCTION

The standard numerical tools for modeling and designing wave energy converters (WECs) rely on linear potential theory [1, 2, 3, 4, 5], and as such are limited to movements of small amplitude around mean positions. However efficiency of WECs relies on large amplitude motion [6]: by design, their resonant frequencies must fall in the wave excitation range. Linear potential theory has been shown to be insufficient to model the behavior of WECs in such configurations [7, 8]. Thus, other numerical approaches are required. A nonlinear potential-flow model, in the context of a numerical wave-tank (NWT), was pioneered by Longuet-Higgins and Cokelet [12]. In their work, they used the mixed Eulerian-Lagrangian (MEL) approach, solving the Laplace equation in an Eulerian coordinate system, and then advecting the nodes at the mesh boundaries. Since that time, several wave tanks have been developed, in both two and three dimensions [13, 14, 15, 16]. Issues related to the development of NWT have been reviewed by Tanizawa [17]. Recent developments have focused on accelerating three-dimensional NWT (computational requirements are still large) and address issues of gridding, numerical stability, and accuracy that can be problematic for complex geometries [18, 19].

A weakly nonlinear approach, based on the weak-scatterer (WS) approximation, is expected to be a promising alternative that avoids or reduces the impediments of fully nonlinar potential-flow codes. Introduced by Pawlowski [9], this class of approximation is based on linearisation of the free surface conditions on the incident wave elevation, allowing treatment of nonlinear steep incident waves. The body condition is evaluated at the exact instantaneous position of the body, allowing large body motions to be taken into account. The only assumption in the WS approach is that the perturbation potential is small. Thus, numerical codes based on the WS approach are expected to be accurate in cases with small to large amplitude body motions, incident waves of arbitrary steepness and when the perturbed wave is small. The different quantities are then decomposed into incident and perturbation components, with the incident ones as forcing terms while only the perturbation ones are solved. The main advantage of this is that the incident wave does not need to be propagated from a wave-maker, allowing the mesh to be refined only in the vicinity of the body. Moreover, since the free surface boundary is known explicitly, the WS method is expected to be more robust and stable than the fully non linear approach.

Several WS flow solvers have been developed in the past: SWAN-4 [20], LAMP-4 [21] and WISH [22]. Their fields of study were however mainly focused on ship with forward speed, which can indeed be considered as slender bodies. As a consequence, the scattered waves and motion responses are small and the assumptions of the WS approximation are fulfilled. In this article, the aim is to investigate whether the WS method can improve numerical modeling of WECs.

The development of this new solver is based on the experience gained by the authors in the 90's in developing a three-dimensional time domain boundary integral equation (BIE) solver for linear, second-order and fully nonlinear wave-body interaction problems [13, 23, 16, 24]. In particular, although higher order BIE solvers are available, the choice of a linear, isoparametric BIE solver based on triangular elements has been maintained. This

solution method presents some important advantages, namely the capacity to express the surface integrals in a purely analytic form, and very good efficiency (typically, the ratio of number of unknowns to number of elements is approximately 0.5). In addition, it is possible to apply efficient mesh generation schemes that originate from the finite element community, which is considered to be key to practical applications. Analytical expressions for the influence coefficients, initially unpublished [25], have been completely redeveloped by the first author during his PhD work, and are presented in Appendix A of this paper.

Comparisons with a fully nonlinear flow solver have been carried out for a submerged body in forced motions [26]. In the present paper, we extend this to the case of freely moving bodies, which requires new equations and numerical implementations to calculate the motion of the body. The Implicit method, introduced by Tanizawa [27] and based on the solution of a second Boundary Value Problem (BVP) for the time derivative of the velocity potential, was chosen to solve the complex implicit problem of the body motion calculations. We have developed a new expression for the BVP body condition, which unifies the two expressions previously given by Tanizawa [27] and Cointe [28] ; the details are presented in [29].

First, WS theory is recalled. The numerical implementations are then introduced, namely the boundary element method, the time-marching scheme and the fluid/structure interaction method. Finally, the method is applied to two submerged WECs, using the Ceto[10] and WaveRoller[11] systems as examples. For the purpose of verification, results are initially compared to linear theory in linear conditions. Simulations in nonlinear conditions, with large amplitude motions and large steepness incident wave, are then conducted.

2. METHODS

2.1. Potential flow theory

Assuming a fluid to be incompressible and inviscid with irrotational flow, its flow velocity derives from a velocity potential ϕ which satisfies the Laplace Eq.:

$$\nabla^2\phi(x,y,z,t) = 0 \tag{1}$$

in the fluid domain, D. The boundary of the fluid domain is $\partial D = \Gamma = \Gamma_{fs} \cup \Gamma_b \cup \Gamma_w \cup \Gamma_d$, see Fig 1.

In the general case, without forward speed, it can be shown [30] that the velocity

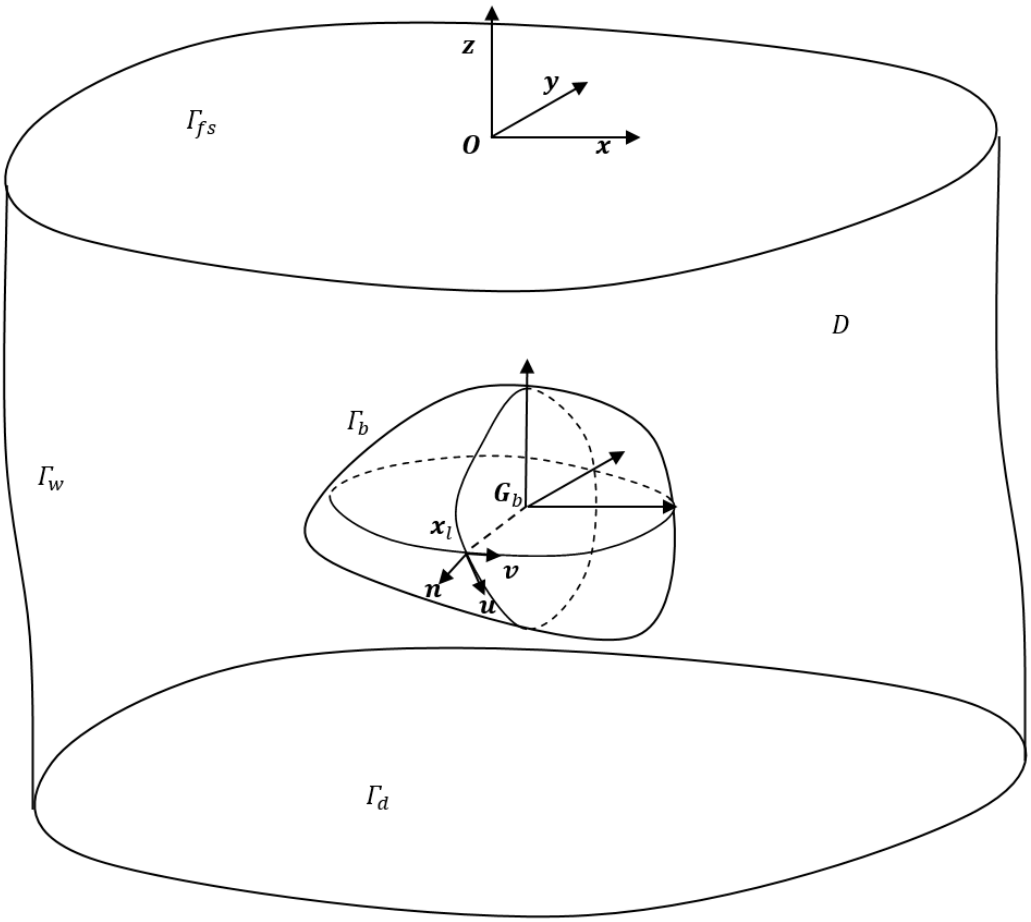

Figure 1: Domain definition : boundaries and reference frames

potential is the solution of the following boundary value problem (BVP):

$$\begin{cases} \nabla^2\phi = 0 & \text{in the fluid domain } D \\ \dfrac{\partial\phi}{\partial t} = -g\eta - \dfrac{1}{2}\nabla\phi\cdot\nabla\phi & \text{on the free surface, } \Gamma_{fs} \\ \dfrac{\partial\eta}{\partial t} = \dfrac{\partial\phi}{\partial z} - \nabla\phi\cdot\nabla\eta & \text{on the free surface, } \Gamma_{fs} \\ \dfrac{\partial\phi}{\partial n} = \mathbf{V_b}\cdot\mathbf{n} & \text{on the body, } \Gamma_b \\ \dfrac{\partial\phi}{\partial n} = \phi_0 & \text{on the seabed, } \Gamma_d \\ \phi \longrightarrow 0 & \text{on boundaries far from the body, } \Gamma_w \end{cases} \tag{2}$$

The free surface elevation is denoted by the single-valued variable η, which means that wave overturning cannot be handled. g is the gravitational acceleration, $\mathbf{V}_b$ the body

velocity and $\mathbf{n}$ the normal vector pointing outwards from the fluid. ϕ_0 is the velocity potential of the incoming waves.

Using Green's Second Identity along with the Rankine source, it can be shown that the resolution of the 3D Laplace equation in the fluid domain can be reduced to a surface integral equation, on its boundaries.

2.2. The weak-scatterer approximation

The WS approximation relies on the decomposition of the velocity potential and the free surface elevation (ϕ, η) into the incident (ϕ_0, η_0) and the perturbation (ϕ_p, η_p) components, see Fig 2.

$$\begin{cases} \phi &= \phi_0 + \phi_p \\ \eta &= \eta_0 + \eta_p \end{cases} \tag{3}$$

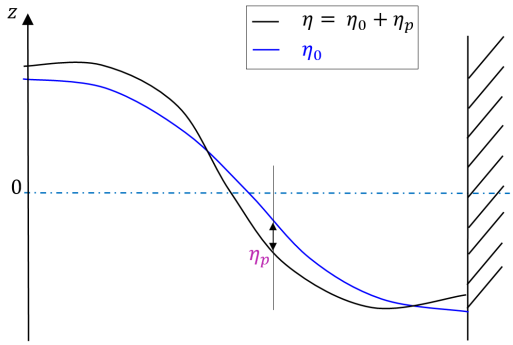

Figure 2: Weak-Scatterer decomposition and definition of the different wave elevation components

The perturbation components are generated by the interaction of the body with the incident (undisturbed) flow. They include diffraction and radiation effects. In the WS approximation, the perturbation components are assumed to be small compared to the incident components.Since the incident components can be considered as forcing terms, only the perturbation components are solved. Thus, the incident wave does not need to be generated using a wave maker on an outer boundary, and propagated with the flow solver. This allows us to refine the free surface mesh only close to the body, which would not have been possible if the incident wave have had to be propagated across the whole computational domain.

The free surface equations can then be linearized on the instantaneous position of the incident wave, which is explicitly known. Since the position of the free surface is independent of the solution, the WS approach is then more robust than the fully non linear approach, in which the free surface position is one of the unknowns.

2.2.1. Incident wave model

In the WS method, the free surface boundary conditions are linearized on the position of the incident free surface. This means that the incident wave model has to fulfill the nonlinear free surface boundary conditions. The chosen model is thus the nonlinear

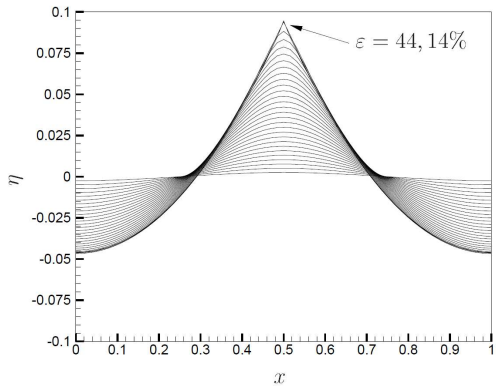

Figure 3: Free surface elevation from stream function solution in deep water for different steepness, from [16]. x is the non-dimensional wavelength, while η is the wave elevation.

solution given by the stream function theory of Rienecker and Fenton [31]. Based on Fourier series, the incident field calculations can be obtained accurately and quickly, for very steep waves, up to the theoretical limit of wave-breaking, see Fig 3. Only regular waves are considered in this study.A coupling with a High Order Spectral (HOS) [32] method may be carried out to take into account more complex nonlinear incident waves (irregular sea states with possible directional spreading).

2.2.2. Free-surface boundary conditions

The fully nonlinear kinematic and dynamic free surface conditions, applied at the exact position of the free surface at $z = \eta$, are:

$$\frac{\partial \eta}{\partial t} = \frac{\partial \phi}{\partial z} - \nabla\phi \cdot \nabla\eta \tag{4}$$

$$\frac{\partial \phi}{\partial t} = -\frac{1}{2}\nabla\phi \cdot \nabla\phi - g\eta \tag{5}$$

In order to make the Mixed Euler-Lagrange (MEL) approach [12] simpler, the free surface nodes are allowed to move only vertically. It is imposed that they follow the incident wave position: a node of coordinates $(x, y, z = \eta_0(x, y, t))$ moves vertically to $(x, y, z = \eta_0(x, y, t+dt))$ with a velocity $\mathbf{v} = \frac{\partial \eta_0}{\partial t}\mathbf{z}$. The corresponding derivation operator is

$$\frac{D_{0z}}{Dt} = \frac{\partial}{\partial t} + \frac{\partial \eta_0}{\partial t}\frac{\partial}{\partial z} \tag{6}$$

Noting that the wave elevation η is independent of z, this leads to $\dfrac{D_{0z}\eta}{Dt} = \dfrac{\partial \eta}{\partial t}$. Introducing the WS decomposition in the kinematic free surface boundary condition, Eq. (4), yields

$$\frac{\partial \eta_p}{\partial t} = -\frac{\partial \eta_0}{\partial t} + \frac{\partial}{\partial z}(\phi_p + \phi_0) - \nabla(\phi_p + \phi_0) \cdot \nabla(\eta_p + \eta_0) \text{ , on } z = \eta(x, y) = \eta_0 + \eta_p \tag{7}$$

A Taylor expansion on the perturbation component η_p (which is small compared to η_0) is applied at the incident free surface position, in order to obtain the WS kinematic free surface condition. The higher order components (η_p^2, ϕ_p^2, $\eta_p.\phi_p$, etc.) are neglected.

$$\begin{aligned}\frac{\partial \eta_p}{\partial t} &= \frac{\partial \phi_p}{\partial z} - \nabla\phi_p \cdot \nabla\eta_0 - \nabla\phi_0 \cdot \nabla\eta_p \\ &\quad + \eta_p \left(\frac{\partial^2 \phi_0}{\partial z^2} - \frac{\partial \nabla\phi_0}{\partial z} \cdot \nabla\eta_0 \right) \text{ , on } z = \eta_0 \end{aligned} \tag{8}$$

The same operations are successively applied to the dynamic free surface equation, to obtain its WS version:

$$\begin{aligned}\frac{D_{0z}\phi_p}{Dt} &= -g\eta_p - \nabla\phi_p \cdot \nabla\phi_0 + \frac{\partial \eta_0}{\partial t}\frac{\partial \phi_p}{\partial z} \\ &\quad - \eta_p \left(\frac{\partial^2 \phi_0}{\partial z \partial t} + \frac{\partial \nabla\phi_0}{\partial z} \cdot \nabla\phi_0 \right) \text{ , on } z = \eta_0 \end{aligned} \tag{9}$$

2.2.3. Body boundary condition

The body condition in the boundary value problem, Eq. 2, is:

$$\frac{\partial \phi}{\partial n}(\mathbf{x}) = \mathbf{V}_b(\mathbf{x}) \cdot \mathbf{n} \tag{10}$$

According to the WS approximation, the wetted surface of the body takes into account the instantaneous incident wave elevation. Introducing the WS decomposition, Eq.(3), in the body condition yields:

$$\frac{\partial \phi_p}{\partial n}(\mathbf{x}) = -\frac{\partial \phi_0}{\partial n}(\mathbf{x}) + \mathbf{V}_b(\mathbf{x}) \cdot \mathbf{n} \quad \text{on the wetted surface of the body, } \Gamma_b \tag{11}$$

The boundary condition on the seabed is similar, with a zero boundary velocity:

$$\frac{\partial \phi_p}{\partial n}(\mathbf{x}) = -\frac{\partial \phi_0}{\partial n}(\mathbf{x}) \quad \text{on the seabed, } \Gamma_d \tag{12}$$

2.2.4. Far-field condition

Far from the origin of the perturbation (the WECs), the perturbation components must vanish:

$$\left\{ \begin{array}{rcl} \eta_p & \rightarrow & 0 \\ \phi_p & \rightarrow & 0 \end{array} \right. \text{ , when } r \rightarrow \infty \tag{13}$$

Our numerical domain is bounded by a vertical cylinder control surface, Γ_w. The incident wave is expected to go through this surface:

$$\frac{\partial \phi}{\partial n}(\mathbf{x}) = \frac{\partial \phi_0}{\partial n}(\mathbf{x}) \quad \text{, on } \Gamma_w \tag{14}$$

leading to the boundary condition:

$$\frac{\partial \phi_p}{\partial n} = 0 \quad \text{, on } \Gamma_w \tag{15}$$

while the control surface is assumed sufficiently far from the body so that the normal velocity of the perturbation velocity potential is negligible. A numerical beach was also applied to ensure this last condition, see section 3.3.

2.2.5. Summary: boundary value problem

The BVP for the velocity potential resulting from the BIE and the previous boundary conditions can thus be described as:

$$\begin{cases} \triangle\phi_p &= 0 & \text{in the fluid domain, } D \\ \dfrac{D_{0z}\phi_p}{Dt} &= -g\eta_p - \nabla\phi_p\cdot\nabla\phi_0 + \dfrac{\partial\eta_0}{\partial t}\dfrac{\partial\phi_p}{\partial z}r & \text{on the free surface,} \\ & \quad -\eta_p\left(\dfrac{\partial^2\phi_0}{\partial z\partial t} + \dfrac{\partial\nabla\phi_0}{\partial z}\cdot\nabla\phi_0\right) & \Gamma_{fs} : z=\eta_0 \\ \dfrac{\partial\eta_p}{\partial t} &= \dfrac{\partial\phi_p}{\partial z} - \nabla\phi_p\cdot\nabla\eta_0 - \nabla\phi_0\cdot\nabla\eta_p & \text{on the free surface,} \\ & \quad +\eta_p\left(\dfrac{\partial^2\phi_0}{\partial z^2} - \dfrac{\partial\nabla\phi_0}{\partial z}\cdot\nabla\eta_0\right) & \Gamma_{fs} : z=\eta_0 \\ \dfrac{\partial\phi_p}{\partial n} &= -\dfrac{\partial\phi_0}{\partial n} + \mathbf{V}_b(\mathbf{x})\cdot\mathbf{n} & \text{on the body, } \Gamma_b \\ \dfrac{\partial\phi_p}{\partial n} &= -\dfrac{\partial\phi_0}{\partial n} & \text{on the seabed, } \Gamma_d \\ \dfrac{\partial\phi_p}{\partial n} &= 0 & \text{on the control surface, } \Gamma_w \end{cases} \tag{16}$$

2.3. Hydrodynamic Force and Body Motions

2.3.1. Equations of motion

The body motion equations are obtained according to Newton's law:

$$\begin{cases} \mathbf{M}\cdot\ddot{\mathbf{x}}_b &= \mathbf{F}_H + \mathbf{M}\cdot\mathbf{g} + \sum\mathbf{F}_{ext} \\ \delta_b = \mathbf{I}_0\cdot\mathbf{S}\cdot\ddot{\theta}_b + \left[\mathbf{I}_0\cdot\dot{\mathbf{S}} + \dot{\mathbf{I}}_0\cdot\mathbf{S}\right]\cdot\dot{\theta}_b &= \mathbf{M}_b(\mathbf{F}_H) + \sum\mathbf{M}_b(\mathbf{F}_{ext}) \end{cases} \tag{17}$$

where $\mathbf{M}$ and $\mathbf{I}_0$ are the mass and inertia matrices, $\ddot{\mathbf{x}}_b$ and $\ddot{\theta}_b$ are the acceleration in translation and rotation of the center of gravity of the body in the global reference frame, $\mathbf{F}_H$ and $\mathbf{M}_b(\mathbf{F}_H)$ and $\mathbf{F}_{ext}$ and $\mathbf{M}_b(\mathbf{F}_{ext})$ are respectively the hydrodynamic and external (Power Take-Off (PTO), mooring, viscous damping, *etc.*) forces and moments applied on the body at its center of gravity, and $\mathbf{S}$ is the rotation matrix based on the Euler angles:

$$\mathbf{S} = \begin{pmatrix} \cos(\theta)\cos(\psi) & -\sin(\psi) & 0 \\ \cos(\theta)\sin(\psi) & \cos(\psi) & 0 \\ -\sin(\theta) & 0 & 1 \end{pmatrix} \tag{18}$$

$$\mathbf{\Omega} = \dot{\psi}\mathbf{z}_0 + \dot{\theta}\mathbf{y}_\psi + \dot{\varphi}\mathbf{x}_\theta = \mathbf{S}\cdot\dot{\theta}_\mathbf{b} \tag{19}$$

where $\mathbf{\Omega}$ is the body rotational vector according to the Euler angles ($\dot{\theta} = \begin{pmatrix}\dot{\psi} & \dot{\theta} & \dot{\varphi}\end{pmatrix}$) (see Fig 4).

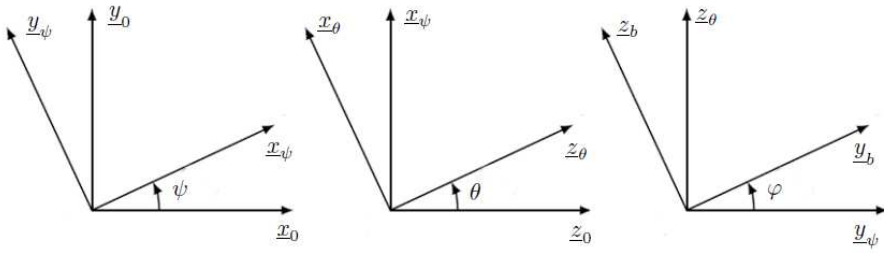

Figure 4: Euler angles (ψ, θ, φ) with their corresponding vectors

The hydrodynamic force and moment are obtained by integrating the hydrodynamic pressure on the wetted body surface (normal vector pointing outwards from the fluid).

The pressure p is given by Bernoulli's equation, and expressed relatively to the atmospheric pressure p_a : $p = \tilde{p} - p_a$. Moreover, the free surface pressure is supposed to be zero:

$$p = -\rho \left(\frac{\partial \phi}{\partial t} + \frac{1}{2} \nabla \phi \cdot \nabla \phi + gz \right) \tag{20}$$

The velocity potential is known on the body, as the solution of the BVP. Its local derivatives are computed using a B-spline approximation of the potential, while the normal velocity is given by the body condition. The velocity potential time derivative is *a priori* not known on the body and needs to be computed.

2.3.2. Velocity Potential Time Derivative

For a body undergoing prescribed motion, the equations of motion, and thus the hydrodynamic loads, do not need to be computed to carry on the simulation. Since the velocity potential is known on the body at each time-step, a finite difference scheme can be used in post-processing, to estimate its time derivative and from this the induced body loads.

For a body undergoing free motion, this scheme is not accurate enough and can lead to instabilities [33]. Another approach has been chosen, based on the solution of a second BVP for the velocity potential time derivative, which also satisfies the Laplace equation [28].

$$\triangle \phi = 0 \Longrightarrow \triangle \frac{\partial \phi}{\partial t} = 0, \text{ in } D \tag{21}$$

The BVP for the time derivative of the velocity potential is similar to that for the velocity potential. The boundary conditions are mixed: Neumann for the material boundaries (body, seabed and numerical control surfaces) and Dirichlet for the free-surface. Since the material derivative $\frac{D_{0z}\phi_p}{Dt}$ is already calculated on the free-surface for the time integration of the free-surface elevation, we can get the partial time derivative of the

velocity potential using Eq.(6)

$$\begin{cases} \triangle \dfrac{\partial \phi_p}{\partial t} = 0 & \text{in the fluid domain, } D \\ \dfrac{\partial \phi_p}{\partial t} = \dfrac{D_{0z}\phi_p}{Dt} - \dfrac{\partial \eta_0}{\partial t}\dfrac{\partial \phi_p}{\partial z} & \text{on the free surface, } \Gamma_{fs} : z = \eta_0 \\ \dfrac{\partial^2 \phi_p}{\partial n \partial t} = -\dfrac{\partial^2 \phi_0}{\partial n \partial t} + \ddot{\mathbf{x}} \cdot \mathbf{n} + q & \text{on the body, } \Gamma_b \\ \dfrac{\partial^2 \phi}{\partial n \partial t} = -\dfrac{\partial^2 \phi_0}{\partial n \partial t} & \text{on the seabed, } \Gamma_d \\ \dfrac{\partial^2 \phi}{\partial n \partial t} = 0 & \text{on the numerical tank walls, } \Gamma_w \end{cases} \tag{22}$$

where $\ddot{\mathbf{x}}$ is the acceleration vectors in translation of the node considered and q represents advection due to the motion of the body. Two different expressions for q have been derived by Cointe [28] and Tanizawa [27] by developing the Neumann condition on moving boundaries using two different kinds of acceleration: respectively, acceleration of the body and acceleration of a fluid particle sliding on the body. The two expression were shown to be equivalent in [29] and a new expression, unifying them, is recalled here:

$$\begin{aligned} q \;=\; & (\boldsymbol{\Omega} \cdot \mathbf{s}_1)\left(\frac{\partial \phi}{\partial s_2} - 2(\dot{\mathbf{x}} \cdot \mathbf{s}_2)\right) - (\boldsymbol{\Omega} \cdot \mathbf{s}_2)\left(\frac{\partial \phi}{\partial s_1} - 2(\dot{\mathbf{x}} \cdot \mathbf{s}_1) -\right) \\ & + \frac{(\dot{\mathbf{x}} \cdot \mathbf{s}_1)}{R_1}\left(\frac{\partial \phi}{\partial s_1} - (\dot{\mathbf{x}} \cdot \mathbf{s}_1)\right) + \frac{(\dot{\mathbf{x}} \cdot \mathbf{s}_2)}{R_2}\left(\frac{\partial \phi}{\partial s_2} - (\dot{\mathbf{x}} \cdot \mathbf{s}_2)\right) \\ & + (\dot{\mathbf{x}} \cdot \mathbf{n})\left(\frac{\partial^2 \phi}{\partial s_1^2} + \frac{\partial^2 \phi}{\partial s_2^2} + \left(\frac{1}{R_1} + \frac{1}{R_2}\right)\frac{\partial \phi}{\partial n}\right) \end{aligned} \tag{23}$$

where $\mathbf{s}_1$ and $\mathbf{s}_2$ are the local coordinate vectors and (R_1, R_2) denote the local curvature along the respective local vectors.

2.3.3. Implicit method

As seen in the previous sections, solution of the equations of motion depends on the calculation of the hydrodynamic force (Eq. (17)), which in turn depends on the calculation of the velocity potential time derivative that is found by solving the solution of the second BVP (Eq. (22)). However, the body boundary condition of this BVP requires knowledge of the acceleration of the body. This leads to an implicit problem, which can be solved using the Implicit method introduced by Tanizawa [27] and Van Daalen [34] for this purpose. The BVP is extended to include the equations of motion and hydrodynamic force calculation, which are then solved simultaneously. $\frac{\partial^2 \phi}{\partial n \partial t}$ and $\frac{\partial \phi}{\partial t}$ on the body are then solutions of this extended BVP, as is the body motion.

Several other methods have been proposed, including the indirect method, the mode decomposition method, and the iterative method (see [35, 36]). The Implicit method requires solving only one additional BVP, compared to up to six for the other methods. Thus, it is expected to be more computationally efficient.

3. NUMERICAL IMPLEMENTATION

3.1. Solution of the BIE

The collocation method is used to solve the BVP. The BIE is thus applied to a set of nodes, $\mathbf{x}_l$, on the boundaries. For given elements j and a field point l, the BIE can be decomposed into two integrals:

$$I_{\sigma,j}(\mathbf{x}) = \iint_{\mathsf{S}_j} \frac{\partial \phi}{\partial n}(\mathbf{x}_l) G(\mathbf{x}, \mathbf{x}_l) d\Gamma \tag{24}$$

$$I_{\mu,j}(\mathbf{x}) = \iint_{\mathsf{S}_j} \phi(\mathbf{x}_l) \frac{\partial G(\mathbf{x}, \mathbf{x}_l)}{\partial n} d\Gamma \tag{25}$$

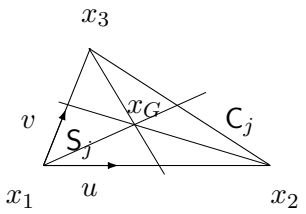

Figure 5: Linear discretization on an element $\mathsf{S}_j = (x_1, x_2, x_3)$: definition of the variables u and v

Linear triangular elements are used, via an isoparametric parametrization, describing both the geometry and the spatial variation of the unknowns (see Fig 5).

$$\begin{aligned} f_j(\mathbf{x}) &= f_j(\mathbf{x}_1) + u(f_j(\mathbf{x}_2) - f_j(\mathbf{x}_1)) + v(f_j(\mathbf{x}_3) - f_j(\mathbf{x}_1)) \\ &= f_j(\mathbf{x}_G) + \nabla_s(f_j) \cdot \mathbf{r_j} \end{aligned} \tag{26}$$

where $\mathbf{x}_G$ is the position vector of the center of gravity G_j of the element $\mathsf{S}_j = (\mathbf{x}_1\mathbf{x}_2\mathbf{x}_3)$, $\mathbf{r_j} = \mathbf{x} - \mathbf{x}_{Gj}$ and $\nabla_s(f_j)$ represents the surface gradient of f_j, which can be calculated from the derivatives of f_j along u and v. C_j is the contour of the element.

Using this discretization, the two integrals can be written as (see AppendixA):

$$I_{\sigma,j}(\mathbf{x}) = \left[\overline{\overline{\Delta}} \iint_{\mathsf{S}_j} G(\mathbf{x}, \mathbf{x}) d\Gamma - \left(\oint_{\mathsf{C}_j} \frac{\mathbf{n} \wedge \mathbf{dl}}{G(\mathbf{x}, \mathbf{x})} \right) \overline{\overline{\Sigma}} \right] \cdot \begin{pmatrix} \frac{\partial \phi}{\partial n}(\mathbf{x}_1) \\ \frac{\partial \phi}{\partial n}(\mathbf{x}_2) \\ \frac{\partial \phi}{\partial n}(\mathbf{x}_3) \end{pmatrix} \tag{27}$$

$$I_{\mu,j}(\mathbf{x}) = \left[\overline{\overline{\Delta}} \iint_{\mathsf{S}_j} \frac{\partial G(\mathbf{x}, \mathbf{x})}{\partial n} d\Gamma - \left(\oint_{\mathsf{C}_j} G(\mathbf{x}, \mathbf{x}) \mathbf{r} \wedge \mathbf{dl} \right) \overline{\overline{\Sigma}} \right] \cdot \begin{pmatrix} \phi(\mathbf{x}_1) \\ \phi(\mathbf{x}_2) \\ \phi(\mathbf{x}_3) \end{pmatrix} \tag{28}$$

where $\overline{\overline{\Delta}} = \frac{\bar{\bar{I}}}{3} + \mathbf{x_G x} \cdot \overline{\overline{\Sigma}}$ and $\overline{\overline{\Sigma}}$ is an operator such that $\overline{\overline{\Sigma}} \cdot \begin{pmatrix} f(\mathbf{x}_1) \\ f(\mathbf{x}_2) \\ f(\mathbf{x}_3) \end{pmatrix} = \nabla_s(f)$.

Analytical solutions for the surface integrals have been given by Guevel [37]. Analytic solutions for the contour integrals with Rankine sources were obtained by considering the contributions of each edge of the triangular panel (see AppendixA).

To calculate influence coefficients in cases where the field point is far from the influencing panel, asymptotic solutions for each integral have been developed to speed up calculations [38].

The BIE applied to the set of nodes, with the collocation methods, results in the following linear system to solve, for a point i on the boundary:

$$\mathbf{G}_{ij}\phi(j) = \mathbf{H}_{ij}\phi_{\mathbf{n}}(j) \tag{29}$$

where ϕ and $\phi_{\mathbf{n}}$ are the velocity potential and normal velocity vectors. The matrix $\mathbf{G}$ includes all integrals of Green's function (Eq. (27)), as well as the solid angle terms along the diagonal, and $\mathbf{H}$ includes all integrals of the normal derivative of Green's function (Eq. (28)). These matrices are called influence matrices. The iterative method GMRES (Generalized Minimal RESsidual method) [39] is used to solve the resulting system efficiently.

Some of the vertices may be located at an intersection between surfaces with non-continuous normal vectors (for instance, vertices at the intersection of the free surface and the body surface, or on sharp corners for non-smooth body geometries). They require special treatment, to take into account the different conditions (Dirichlet/Neumann or different normal velocity and normal definition). All the boundary conditions on these particular points are applied by duplicating nodes. For a given geometrical location, several boundary conditions are enforced, to arrive at different solutions.

The continuity of the potential at the intersection is checked to ensure the validity of the BVP solution.

3.2. Code acceleration

Three techniques have been developed to reduce the number of unknowns in the calculation of the influence matrices (and hence the calculation time): partial calculation of the influence matrices; symmetries; and open domain.

- Partial calculation involves calculating the influence matrices only on sub-domains that have changed during the previous time step. A fixed boundary during the simulation does not need to have its auto-influence matrices updated at each time step.

- Two symmetries are implemented, one vertical along the (xOz) plane, and the other horizontal on the bottom (for flat sea bottoms). The two symmetries can be used concurrently. By cutting the number of mesh elements by a factor two, the calculation time for the influence coefficients is also cut by a factor of two, whilst the calculation time for solving the linear system is cut by a factor four.

- Simulations in open domain are also possible, by considering numerical control surfaces to be sufficiently far from the body, so that the perturbation dies out before reaching these boundaries. A classic numerical beach is used to enforce this last condition.

More details concerning these features can be found in [38].

3.3. Numerical beach

We implemented a classic numerical beach [33], based on elongation of the elements on the free surface and the addition of virtual pressure terms in the free surface equations. For the fully nonlinear free surface equations, for example, the method yields:

$$\left\{ \begin{array}{rcl} \dfrac{\partial \phi}{\partial t} & = & -g\eta - \dfrac{1}{2}\nabla\phi \cdot \nabla\phi + \nu\phi \\ \dfrac{\partial \eta}{\partial t} & = & \dfrac{\partial \phi}{\partial z} - \nabla\phi \cdot \nabla\eta + \nu\eta \end{array} \right. \tag{30}$$

For circular domains, the damping variable ν varies as

$$\left\{ \begin{array}{rcll} \nu(r) & = & \alpha\omega \left(\dfrac{(r - r_0)}{\lambda} \right)^2 & r \geq r_0 = R_e - \beta\lambda \\ \nu(r) & = & 0 & r < r_0 \end{array} \right. \tag{31}$$

α and β are parameters that adjust the virtual pressure loads and the width of the numerical beach to the perturbation, respectively, and R_e is the external radius delimiting the free surface in the horizontal plane. $\alpha = 0.7$ and $\beta \simeq 1$ were found to be optimal.

3.4. Local derivative calculations

Spatial derivatives are present in the free surface equation, but also in the q-term of the body condition for the time derivative of the velocity potential BVP (Eq. (23)). The second-order derivatives are also required in this calculation. The local derivatives given by the linear discretization are constant on each element, requiring a special scheme for the evaluation of the second-order derivatives. Following [40], a higher order B-Splines approximation has been implemented, allowing easy calculation of the first- and second-order local derivatives as well as better precision than achieved by the linear discretization, resulting in a low CPU-time cost. Virtual nodes are used to cope with discontinuities in the plane of symmetry.

3.5. Time Integration

A fourth-order Runge-Kutta scheme with a constant time step is used for time-marching . The velocity potential and wave elevation on the free surface are advanced in time using equations Eq. (8) and Eq. (9). The body position and velocity are advanced simultaneously using the body motion equation Eq. (17). The algorithm implies the solution of the BVP for four different mesh configurations during each time step. This theoretically leads to four calculations of the influence matrices.

In practice, it has been observed that it is possible to keep the geometry (free surface and body) during the four substeps of the RK4. This is referred to as geometry-locked-RK4 [13], and results in only one calculation of the influence matrices per time-step. A time convergence of the normal and geometry-locked-RK4 showed that, for a given accuracy, the geometry-locked-RK4 leads to a significant reduction in computational time. Thus, the modified scheme is used in the following.

4. Validation : simulation of a submerged heaving WEC

In this section, the results of the CN_WSC for free-body motions are verified at first in linear conditions (*i.e.* small amplitudes of body motion and wave steepness). Linear potential flow theory is used as a reference, thanks to the open source software Nemoh [41]. Subsequently, nonlinear conditions (*i.e.* large amplitudes of body motion and wave steepness) are studied and differences with linear theory are highlighted. The stiffness of the power take-off is tuned to the wave excitation, to obtain a mechanical resonance. A Fourier analysis is applied to the motion time history, and the mean absorbed power is calculated on several periods of the wave excitation, once the steady state is obtained. Using this methodology, we can obtain normalized responses for the motion and absorbed power for a set of frequencies. These normalized responses can be compared to the linear solutions, *i.e.* the response amplitude operator (RAO). The limits of the WS approximation are also inspected, with respect to the underlying assumptions.

4.1. WEC description

The submerged heaving WEC (SHWEC) that served as the model for this section is the Ceto WEC, designed by Carnegie Wave Energy Limited [10]. This WEC consists of a heaving submerged buoy, moored at the seabed. Here we consider a simplified, neutrally buoyant spherical buoy (see Fig. 6, with a spring-linear damping system to model the mooring and power take-off (PTO). The dimensions are: radius $a = 3.5$ m, mean immersion $d = 2a = 7$ m, depth $H = 20$ m. The spring specifications, K_{PTO} and l_0, are optimized to adjust the body response to the wave input, A_ω and ω. In order to obtain resonant motions, the spring constant is set to $K_{PTO} = (M + \mu_{33})\omega^2$, with μ_{33} given by the linear solution. Linear Power Take-Off (PTO) damping is taken into account. The instantaneous power and energy absorbed by the PTO are:

$$\left\{ \begin{array}{rcl} P_{PTO}(t) & = & B_{PTO}\mathbf{V}(t)^2 \\ \\ E_{PTO}(t) & = & \int\limits_0^t P_{PTO}(\tau)d\tau \end{array} \right. \tag{32}$$

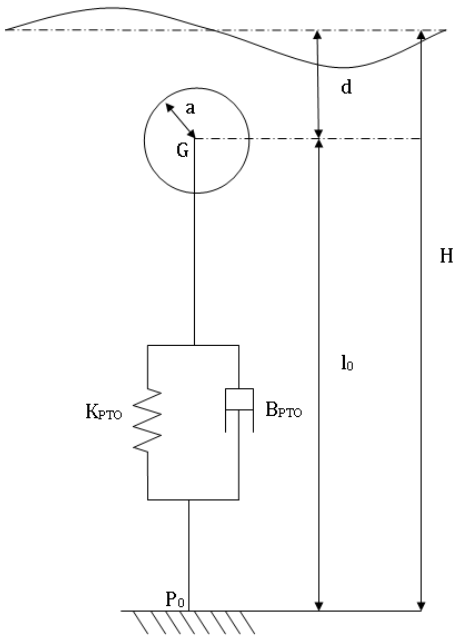

Figure 6: diagram of the SHWEC and its geometrical characteristics

The mean absorbed power P_{abs}, capture width C_W and efficiency η_1, along with the wave energy flux J for a regular wave, are defined as

$$\begin{cases} P_{abs} = \dfrac{E_{PTO}}{t} \quad W \\ C_W = \dfrac{P_{abs}}{J} \quad m \end{cases} \qquad \begin{cases} J = \dfrac{\rho g^2}{8\pi} A_\omega^2 T \tanh(kh)\left(1 + \dfrac{2kh}{\sinh(2kh)}\right) \quad W/m \\ \eta_1 = \dfrac{C_W}{2a} \end{cases} \tag{33}$$

The numerical tank consists in a cylindrical and regular domain, centered around the body, see Fig.7. Vertical and bottom symmetries are used to reduce the numbers of nodes. The radius of the numerical domain varies according to the incident wave length, $R_{Dom} = 3\lambda$ with a numerical absorbing beach radius of one wave length. Based on successful mesh and time convergence studies, the time and space discretisation was chosen such that $dt = T/100$ and $dr = \lambda/20$ or $dr = 0.5m$ for large λ, dr being the size of the smallest elements of the mesh (on the body and on the free surface close to the body).

4.2. Linear conditions

The incident wave considered is a small amplitude regular wave, in order to allow comparisons with linear theory. The wave parameters (angular frequency ω, period T, length λ, amplitude A_ω and steepness $\epsilon = kA_\omega$) are given in Table 1.

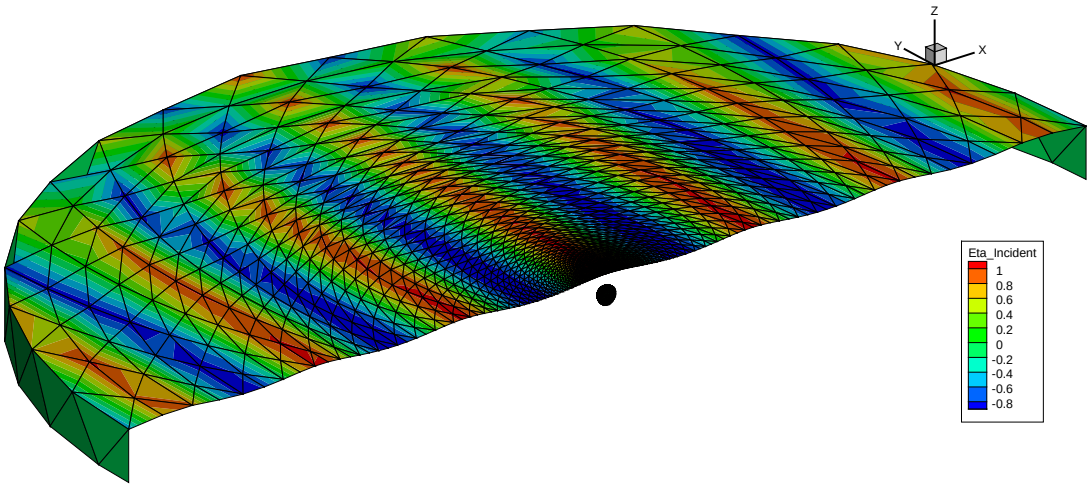

Figure 7: Representation of the numerical domain for the SHWEC

$\omega\ (rad/s)$	$T\ (s)$	$\lambda\ (m)$	$A_\omega\ (m)$	$\epsilon\ (\%)$
1.7	3.7	21.3	0.001	0.03

Table 1: Wave parameters in linear conditions

The small wave amplitude ensures linear conditions: the wave steepness is very small, as is the body motion response, despite the fact that the value of the spring constant was chosen to achieve mechanical resonance, $K_{PTO} = 7.4\ 10^5$ N/m.

Initially, the PTO damping, B_{PTO}, was set to zero, in order to check the radiation damping of the body. The linear and WS solutions of the body heaving motion are plotted in Fig. 8.

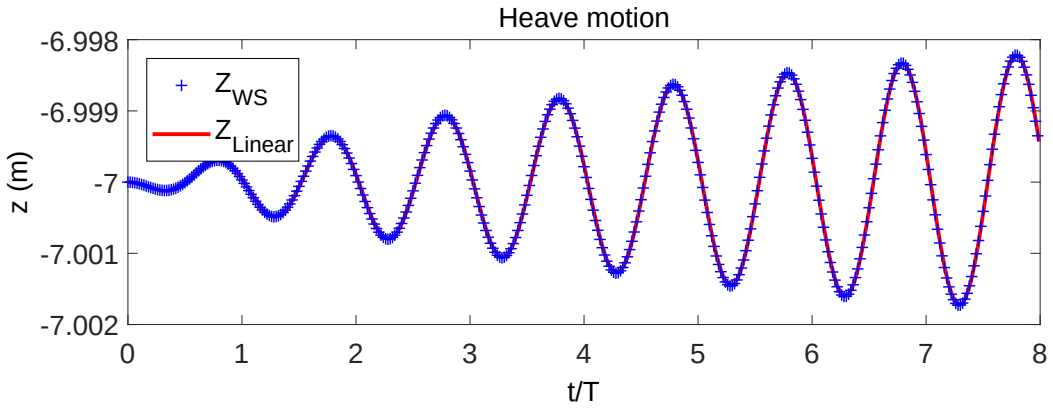

Figure 8: Linear and WS heave motion responses, in linear conditions ($\omega = 1.7$ rad/s, $A_\omega = 0.001$ m, $k_{PTO} = 7.410^6$ N/m, $B_{PTO} = 0$ kg/s)

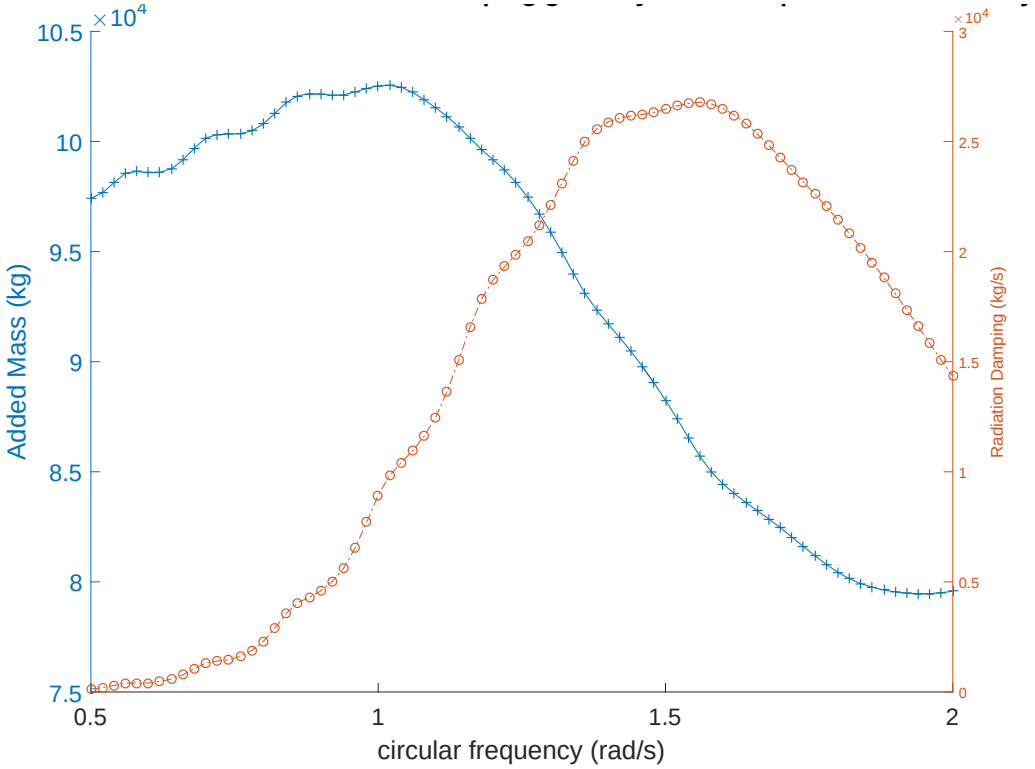

Figure 9: Added Mass and Radiation Damping in Heave for the SHWEC, given by the linear potential flow theory.

Excellent agreement between the linear and WS solutions is observed. Harmonic analysis could not be performed, since the steady state was not achieved due to the small damping. Nevertheless, the agreement validates the implementation of the equations in the WS code.

The PTO damping was then set to $B_{PTO} = 5.10^4$ kg/s, while keeping all other parameters constant. This value is approximately twice the maximum of the radiation damping of the SHWEC, see Fig. 9. A steady state was achieved after approximately five wave periods. In addition to heave motion, the accumulated absorbed energy through the PTO is plotted both for the linear and WS solutions in Fig. 10.

As for the previous case, good agreement between linear and WS solutions was obtained in linear conditions. A small accumulated error in the absorbed energy can be observed, which leads to an offset between the two solutions. It is believed that this is due to the different starting procedures in the two numerical approaches or an accumulated numerical error.

The mean absorbed power, capture width and WEC efficiency were calculated on the three periods after the steady state was reached and compared in Table 2. The wave energy flux per unit length of wave front related to this incident wave is $J = 0.014$ W/m.

The relative errors in the WEC performance values between the linear and WS results

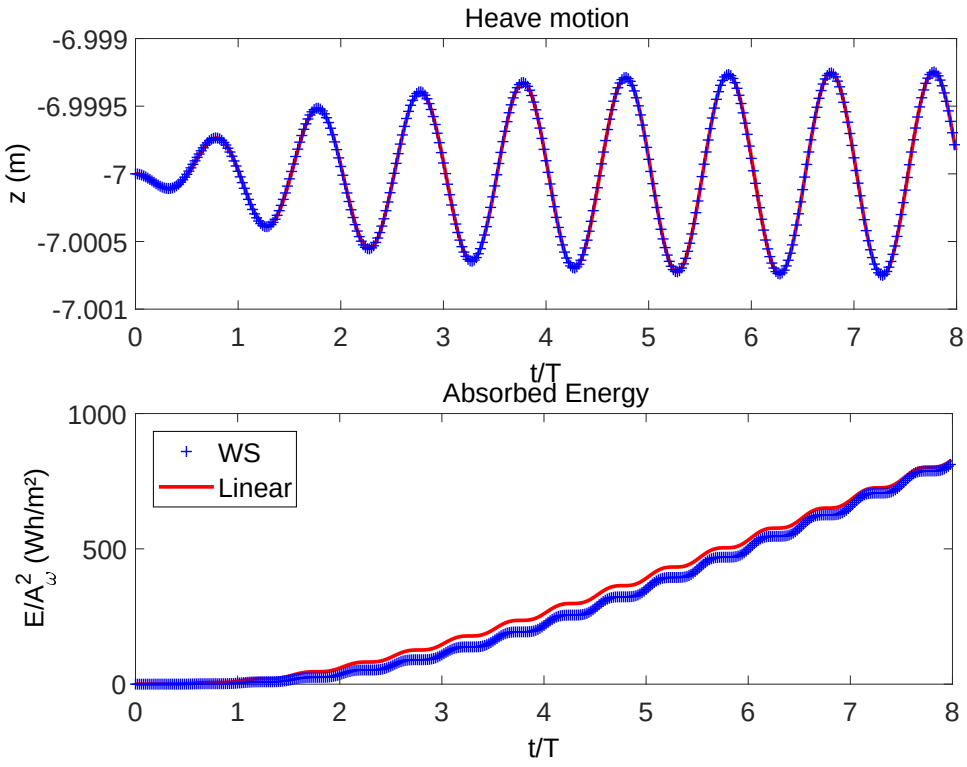

Figure 10: Linear and WS heave motion and absorbed energy, in linear conditions ($\omega = 1.7$ rad/s, $A_\omega = 0.001$ m, $k_{PTO} = 7.410^6$ N/m, $B_{PTO} = 5.10^4$ kg/s)

	P_{abs} (W)	B_J (m)	η_1 (%)
Linear Theory	0.0369	2.61	37.3
CN_WS	0.0367	2.59	37.0

Table 2: Mean absorbed power, capture width and WEC efficiency given by the linear and WS solutions, in linear conditions

are less than 1% validating the implementation of the wave-body motion coupling in the WS code.

The body motion and power output responses were then considered for a set of incident wave angular frequencies, ranging from 0.4 to 2 rad/s. The wave amplitude and PTO damping were kept constant ($A_\omega = 0.001$ m, $B_{PTO} = 5.10^4$ kg/s, respectively). The stiffness constant was tuned for each frequency in order to achieve resonance. The body is meshed using approximately 2000 nodes and the free surface between 1000 and 1600 nodes, depending of the incident wavelength. The resulting computational time per wave period is $T_{CPU}/T \simeq 800$. The geometrical error on the body, due to the meshing, is below 1%. The body motion and power output responses are shown for the two solutions in Fig. 11. The maximum recoverable power for an axisymmetric absorber in heave J/k

is also plotted for comparison.

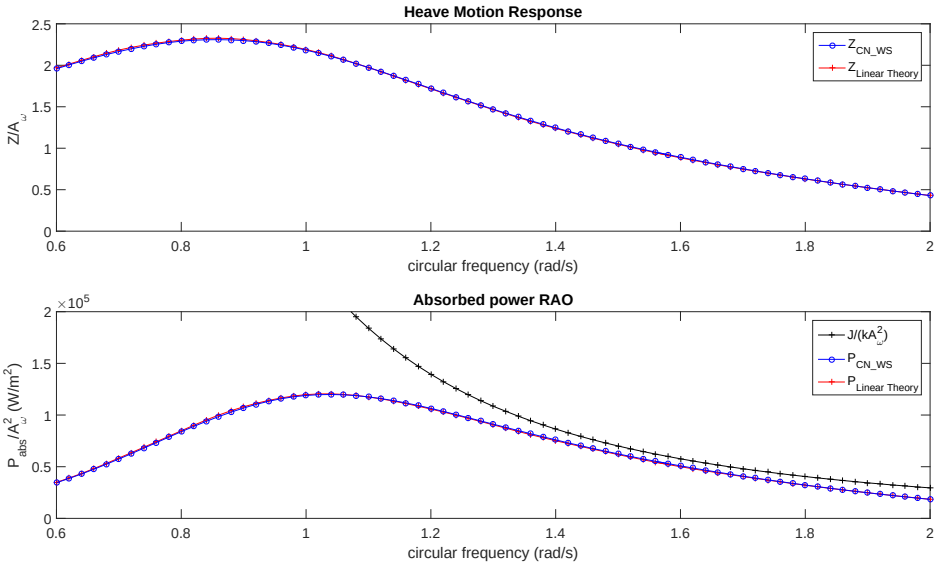

Figure 11: SHWEC motion and power output responses, in linear conditions ($A_\omega = 0.001$ m, $B_{PTO} = 5.10^4$ kg/s, the stiffness K_{PTO} is tuned to adjust the natural frequency to the wave excitation).

Perfect agreement can also be observed between the linear and WS results across the whole range of frequencies. This validates the WS model.

4.3. Nonlinear conditions

With the WS code, two different kinds of nonlinearity can be taken into account and studied. The first relates to the change in body geometry and position relative to the free surface. The second relates to the steepness of the incident wave. These are usually related, since large wave amplitudes lead to large body motions, and hence it is difficult to quantify the effect of one nonlinearity as distinct from the other. For this reason, we first present the normalized responses in heave, and mean absorbed power, for the same body parameters (radius $a = 3.5$ m and submergence $d = 7$ m). The range of angular frequencies is still 0.4 rad/s to 2 rad/s, but the wave amplitude is now equals to 0.85 m; it follows that the wave steepness ranges from 2.6% to 31%. Similar PTO parameters are used: the stiffness is tuned to achieve resonance with the wave frequency, while the damping is kept constant at $B_{PTO} = 5.10^4$ kg/s.

The domain is meshed the same way as in linear conditions : with 2000 nodes on the body and between 1000 and 1600 on the free surface depending on the incident wavelength.

The linear and WS results show significant differences in these nonlinear conditions. These discrepancies are most notable on two ranges of angular frequency. The first is frequencies greater than 1.3 rad/s, *i.e.* wave steepness greater than 20%. These differences are thus related to the incident wave nonlinearities that are taken into account in the

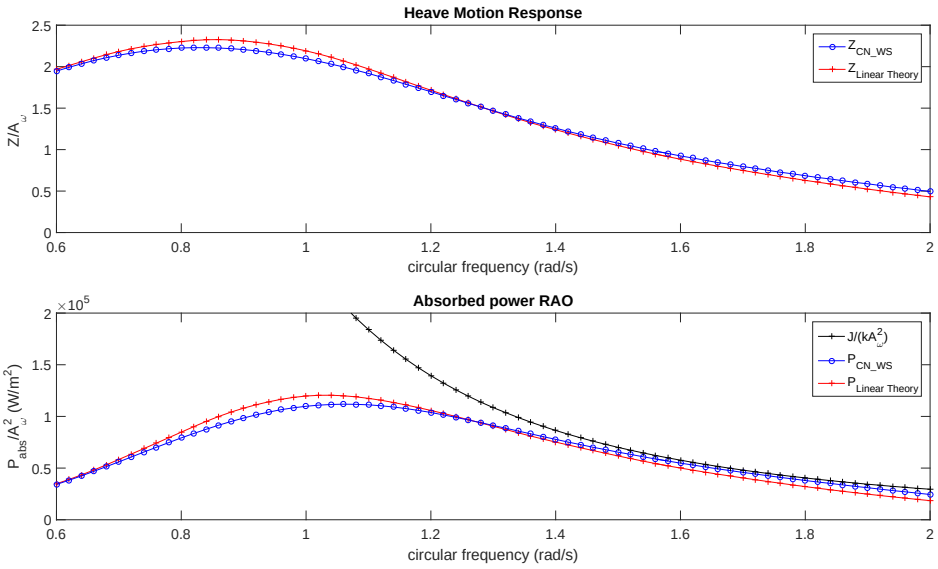

Figure 12: SHWEC motion and power output normalized responses, in nonlinear conditions (A_ω = 0.85 m, $B_{PTO} = 5.10^4$ kg/s and stiffness tuned to adjust the natural frequency to the wave excitation)

WS approximation. With a constant PTO damping for all the frequencies, the lowest normalized response in heave are obtained for this range of frequencies. An interesting result is that linear theory tends to underestimate up to 15% the RAO in heave and 30% the mean absorbed power, compared to the WS approximation, for this range of frequencies. However, with a PTO damping tuned for each frequency, we should be able to get the maximum recoverable energy (J/k) with both linear and WS approximation. The discrepancies between linear and WS solutions are then expected to be smaller in this condition.

The second range of frequencies is between 0.8 rad/s and 1.3 rad/s. The wave steepness in this case is lower than 15%, which means there are fewer wave nonlinearities. In contrast, with the RAO in heave exceeding 2, body nonlinearities are important. The implication is that the RAO in heave, and thus mean absorbed power, tend to be overestimated by linear theory, up to 4.5% and 9% respectively.

Since higher performance is achieved in this second range of frequencies, the WEC will be designed to work mainly in this range, leading to an overestimation of the performance of the WEC by the linear theory. However, this is dependent on the geometrical parameters of the body: the nonlinearities related to large wave amplitude and large motion responses are not always as distinct as here. This decoupling in our case allows us to study the two kind of non linearities separately.

4.3.1. Motion nonlinearities

Motion nonlinearities are studied first, for the angular frequency giving the highest motion response. The wave characteristics and PTO parameters are given in Table 3.

$\omega\ (rad/s)$	$T\ (s)$	$\lambda\ (m)$	$A_\omega\ (m)$	$\epsilon\ (\%)$	$k_{PTO}\ (N/m)$	$B_{PTO}\ (kg/s)$
1	6.3	60	1	13%	3.10^5	5.10^4

Table 3: Wave and PTO parameters producing the highest motion response

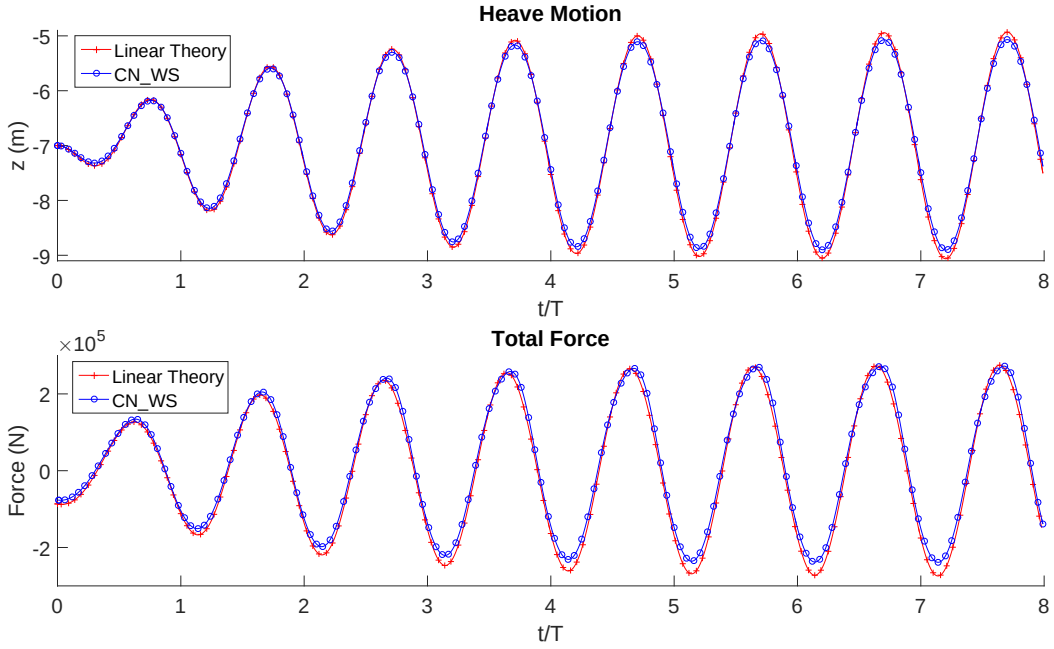

Figure 13: Linear, and WS heave motion, force responses, in a large motion case ($\omega = 1$ rad/s, $A_\omega = 1$ m, $k_{PTO} = 3.10^6$ N/m, $B_{PTO} = 5.10^4$ kg/s)

The linear condition of small motions is not respected: by the end of the simulation, the motion amplitude reaches up to 2 m (50% of the buoy radius a). This results in clear differences between the two approaches: the steady state response amplitude is overestimated by linear theory. Nonlinearities are also visible in the hydrodynamic force. When the body moves close to the free surface, the peaks are deformed in comparison with the linear solution. This arises from a local modification of the radiation damping, leading to a small phase shift for a short time. When the body moves further from the free surface, the radiation damping, and thus the phase shift, return to their mean value. These nonlinearities are thus completely related to the nonlinearities in the body position rather than the large wave amplitude.

These nonlinearities affect the mean absorbed power significantly. Table 4 summarizes the different quantities related to energy absorption, calculated in the same manner as in linear conditions, for the linear and WS approximations. For the incident wave chosen, the wave energy flux is $J = 24.1$ kW/m.

The differences between the two numerical approaches in their calculation of mean absorbed power, and thus also capture width and capture width ratio, are substantial:

	P_{abs} (kW)	B_J (m)	η_1 (%)	t_{CPU}/T
Linear Theory	107	4.44	63	< 1
CN_WS	93	3.85	55	700

Table 4: Mean absorbed power, capture width and efficiency, for the linear and WS approximations, in a large motion case ($\omega = 1$ rad/s, $A_\omega = 1$ m, $k_{PTO} = 3.10^6$ N/m, $B_{PTO} = 5.10^4$ kg/s)

linear theory, which does not take into account the large body motion, overestimates the performance of the WEC, yielding results that exceed those produced by the WS approximation by nearly 15%.

This large wave amplitude, however, pushes our WS flow solver to its limit: the body is almost reaching the free surface. More importantly, the validity of the WS assumption needs to be checked. The incident and perturbation components of the wave elevation are thus plotted in Fig. 14 for a point on the free surface and above the sphere center.

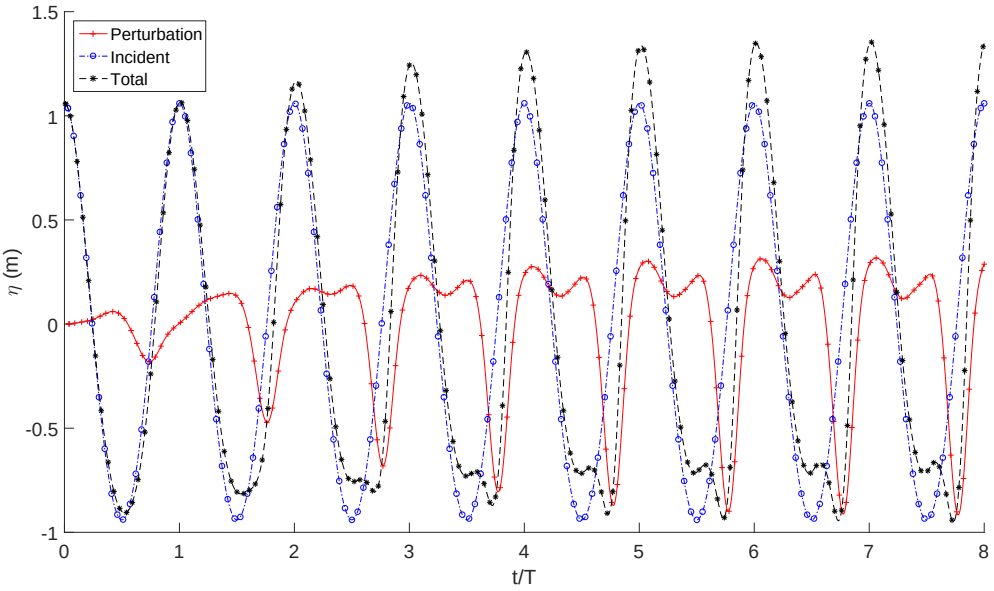

Figure 14: Incident and perturbation wave elevation, above the SHWEC gravity center, in a large motion case ($\omega = 1$ rad/s, $A_\omega = 1$ m, $k_{PTO} = 3.10^6$ N/m, $B_{PTO} = 5.10^4$ kg/s)

The total wave elevation is similar to the incident wave elevation, but demonstrates more nonlinearities (higher peaks, flatter troughs and some higher order components). These differences, which arise from from the perturbation component, are relatively small compared to the incident wave elevation. They are related to the emission of small waves, when the body comes close to the free surface. These waves die out quickly, and hence their maximum amplitude occurs directly above the sphere - which is where the data plotted in Figure 14 were recorded. The WS condition that the perturbation wave elevation should be small compared to the incident wave elevation is not fulfilled in this

specific case. However this hypothesis is also a condition of linear theory, which further requires that amplitude of motion should be small, which is also not the case here. The WS approximation is thus likely to present more accurate physical results than the linear theory.

4.3.2. Wave nonlinearities

Next, we investigated wave nonlinearities, *i.e.* waves with large steepness and relatively small body motion response. The wave characteristics and PTO parameters chosen are given in Table 5. The mean immersion is decreased to $d = 5$ m, in order to increase

ω (rad/s)	T (s)	λ (m)	A_ω (m)	ϵ (%)	k_{PTO} (N/m)	B_{PTO} (kg/s)	d (m)
2	3.14	17	0.85	31%	$9.5.10^5$	5.10^4	5

Table 5: Wave and PTO parameters in steep waves

the influence of the nonlinearities from the wave.

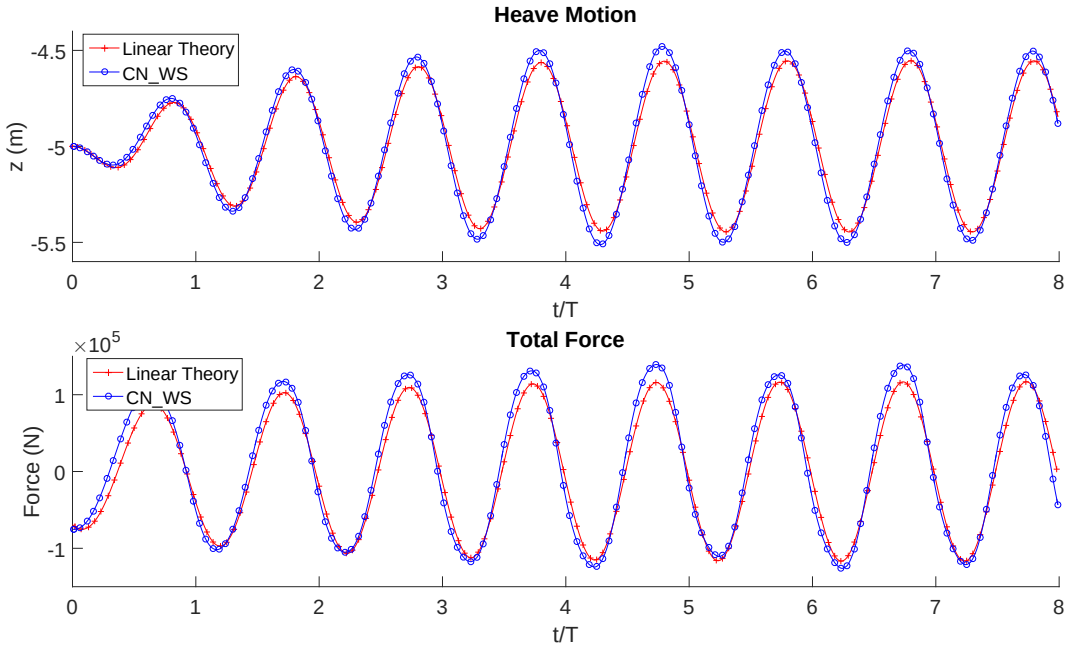

Figure 15: Linear, WS heave motion, force, in a steep wave case ($\omega = 2$ rad/s, $A_\omega = 0.85$ m, $k_{PTO} = 9.510^5$ N/m, $B_{PTO} = 5.10^4$ kg/s, $d = 5$ m)

The linear, WS solutions of the response in heave motion and diffraction-radiation forces are plotted in Fig. 15. The small amplitude motion response assumption is valid in this case: the heave motion maximum amplitude is 0.5 m (0.15a). However, the incident wave approximation differs between the two methods. This is clearly visible in the force response, where the WS solution features higher peaks and flatter troughs than the linear

solution. The Froude-Krylov force, not plotted, displays similar differences between the two solutions. This directly affects the motion response (smaller for the linear theory) and hence the absorbed energy.

Table 6 summarizes the different quantities related to the energy absorption, calculated in the same manner as in linear conditions, for the two approximations. For the selected incident wave, the wave energy flux is $J = 8.7$ kW/m.

	P_{abs} (kW)	B_J (m)	η_1 (%)	t_{CPU}/T
Linear Theory	19.7	2.27	32	< 1
CN_WS	25.3	2.91	42	800

Table 6: Mean absorbed power, capture width and efficiency, for the linear and WS approximation, in a steep wave case ($\omega = 2$ rad/s, $A_\omega = 0.85$ m, $k_{PTO} = 9.510^5$ N/m, $B_{PTO} = 5.10^4$ kg/s, $d = 5$ m)

Linear theory, which does not take into account nonlinear waves, predicts lower performance in steep waves. This result is unexpected.

Again it is important to study the validity of the WS hypothesis in this case. To this end, the incident and perturbation wave elevations are plotted in Fig. 16 where the diffraction is the largest, approximately one wave length after the SHWEC. The linear incident wave elevation, used in linear theory, is also plotted to illustrate differences arising from the incident wave model.

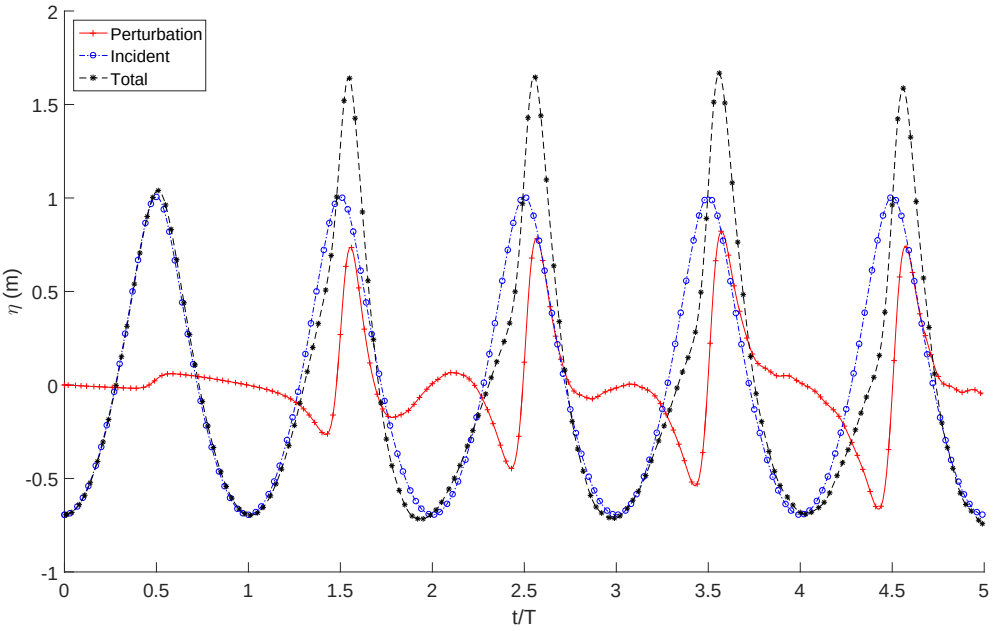

Figure 16: Incident (linear and nonlinear) and perturbation wave elevations, one wave length after the SHWEC, in a steep wave case ($\omega = 2$ rad/s, $A_\omega = 0.85$ m, $k_{PTO} = 9.510^5$ N/m, $B_{PTO} = 5.10^4$ kg/s, $d = 5$ m)

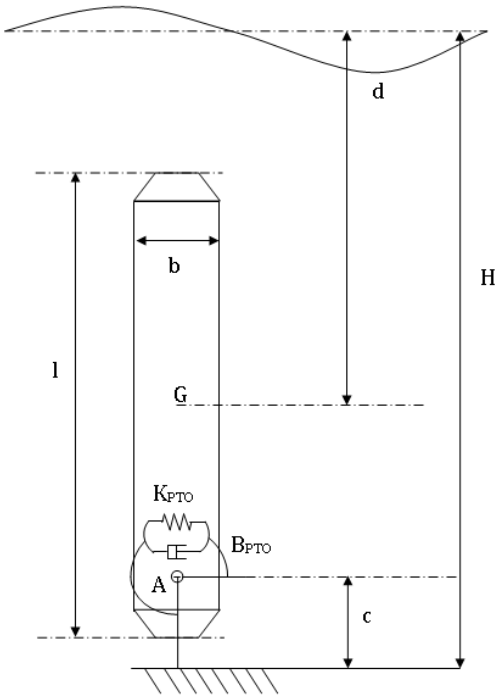

Figure 17: Diagram of the SOWSC and its geometrical characteristics

After a few periods, the perturbation wave elevation is locally almost as large as the incident wave elevation. The total wave (sum of incident and perturbation) is a larger but steeper wave, which is highly likely to break. This phenomenon is related to the emission of small waves due to the diffraction, when the body is close to the free surface. In this case, the fundamental assumption of WS -that the perturbation is small compared to the incident wave elevation - is not respected. However, again, this is also an assumption of linear theory, which further requires the incident wave to be linear (small steepness), a condition that is not fulfilled either.

Thus the validity of the WS hypothesis must be questioned. However, by taking into account nonlinearities, it at least offers a better model of the physics than linear theory.

5. Application to a submerged oscillating wave surge converter

5.1. WEC description

The submerged oscillating wave surge converter (SOWSC) that served as inspiration for this section is the WaveRoller WEC, developed by AW-Energy [11]. Located near-shore (8-20m depth), it consists of a flap attached to the seabed along one edge. This edge becomes an axis around which the flap rotates in a back and forth motion under the influence of the wave surge. A half-scale device was installed in open sea in 2007. An array of three prototypes was deployed in Portugal in 2009.

The PTO of the device is modeled here in its simplest form, as in the previous case, using a linear model including stiffness and damping terms. The shape and dimensions of the device are informed by the latest design, see Fig. 17 and Table 7. The water depth is $H = 9$ m.

height (m)	width (m)	thickness (m)	rotation center (m)	immersion (m)
$l = 6$	$a = 4$	$b = 1$	$c = 2.5$	$d = 5$

Table 7: SOWSC geometrical characteristics

As for the Ceto, the PTO specifications, spring stiffness and damping coefficient, are chosen in such a way as to achieve both resonance for each wave frequency $K_{PTO} = (I_{55} + \mu_{55})\omega^2$ and a short transient response ($< 8T$). The added inertia μ_{55}, required for estimation of the resonance frequency, is given by the linear model.

The PTO damping also being linear, the instantaneous power is simply given by:

$$P_{PTO}(t) = B_{PTO} \times \dot{\theta}(t)^2 \tag{34}$$

The numerical tank is similar to that used for the SHWEC case (see Fig.18). Mesh and time convergence studies showed no difference to the SHWEC case, so the same time and space parameters are used. The body and free surface are meshed using approximately 1200 and 1800 nodes respectively, leading to a mean computational time per wave period of $T_{CPU}/T = 600$.

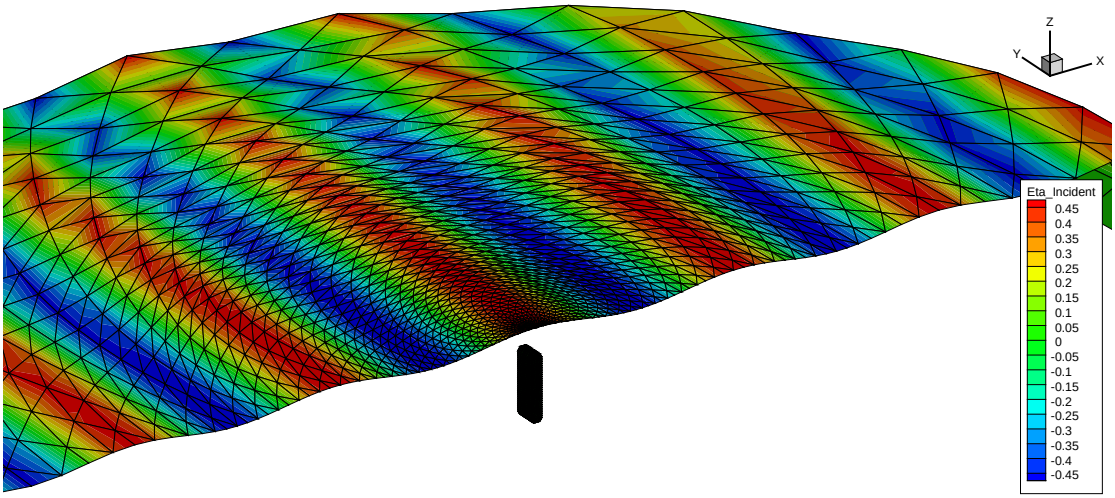

Figure 18: Representation of the numerical domain for the SOWSC

5.2. Linear conditions

The first case considered is small amplitude incident waves. The motion and power responses are calculated for frequencies ranging from $\omega = 0.42$ to 2 rad/s, with a wave amplitude $A_\omega = 0.001$ m. The wave steepness, $\epsilon = kA_\omega$, is thus less than 0.04% for all

frequencies. The motion and power responses are calculated using a Fourier analysis and plotted in Fig. 19.

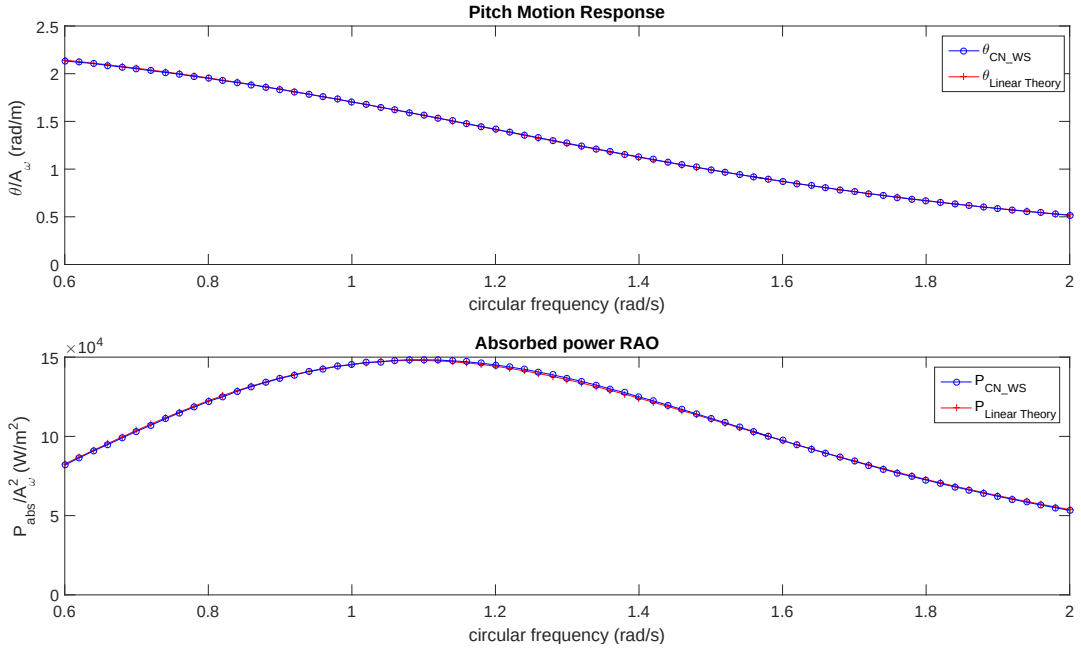

Figure 19: SOWSC Motion and power responses, in linear wave conditions ($A_\omega = 0.001$ m, $B_{PTO} = 5.10^4\ kg.m^2/s$, the stiffness K_{PTO} is tuned to adjust the natural frequency to the wave excitation)

The motion and power responses show excellent agreement between WS and linear results in linear conditions; for the power response, the difference is less than 1%.

5.3. Nonlinear conditions

To compare the methods under nonlinear conditions, the wave amplitude was then set to $A_\omega = 0.5$ m, causing the wave steepness to vary in the range 3.4% to 20.4%. Again, the motion and power responses were predicted for the two numerical approaches, as depicted in Fig. 20.

Significant differences between the two approaches are now observed: at its peak, the power response predicted by the linear approach is nearly 200% that predicted by the WS approach. Since the angular motion RAO ranges between 0.5 to 1.5 rad/m, with a wave amplitude of $A_\omega = 0.5$ m, it follows that the total angular compass of the flap is between 10 to 40°, while the trajectory of the top of the flap ranges from 1.4 m to 4.1 m. These motions are large compared to the dimensions of the flap, leading to nonlinearities that are not taken into account by the linear model. Some of these nonlinearities are a consequence of the small depth that is a characteristic of the SOWSC; however, the large amplitude motion seems to be the predominant source of nonlinearities in this case.

Since linear theory does not take into account these important body motion nonlinearities, linear theory overestimates energy performance for this type of WEC. However,

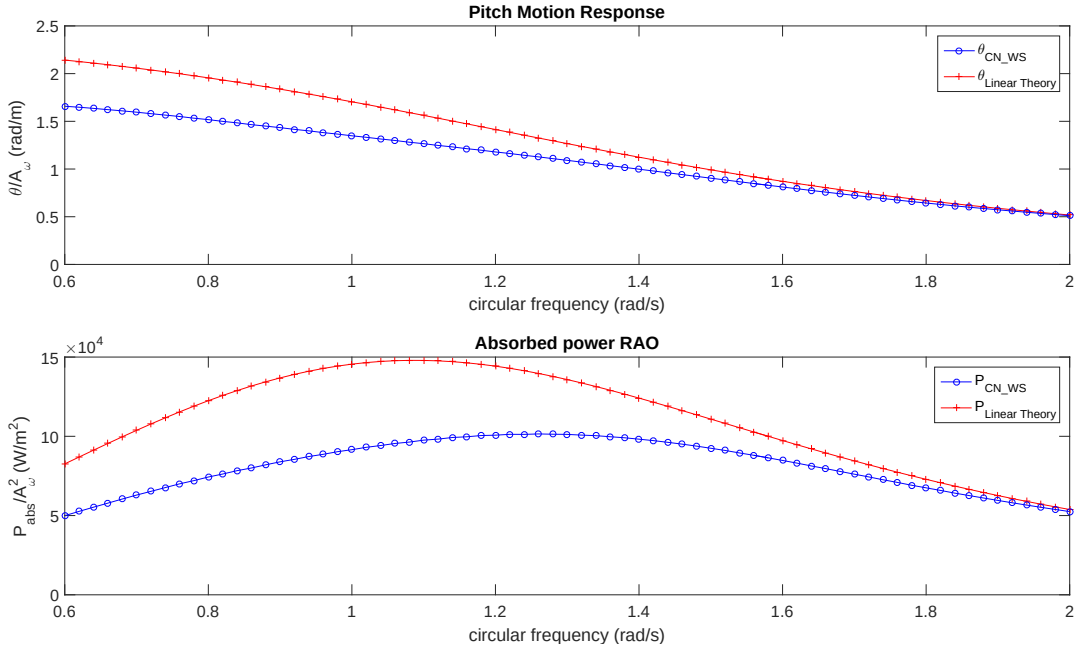

Figure 20: SOWSC Motion and power responses, in nonlinear conditions($A_\omega = 0.5$ m, $B_{PTO} = 5.10^4\ kg.m^2/s$, the stiffness K_{PTO} is tuned to adjust the natural frequency to the wave excitation)

it may be that this is highly dependent on the choice of PTO stiffness (that was tuned in this study in order to achieve resonance for each incident wave frequency).

The validity of the WS assumption is checked in Fig. 21, for $\omega = 0.8$ rad/s. Perturbation waves emitted from the body can become as large as the incident wave, primarily because of the large body motions. In fact it is possible to observe two peaks per period, related to the body approaching the free surface twice per cycle. The total wave elevation is still globally similar to the incident wave elevation, but demonstrates more pronounced nonlinearities. Hence, the assumption of WS, that the perturbation should be small compared to the incident wave elevation, might not be fulfilled locally. However, again, this is also an assumption of the linear theory, which further requires the amplitude of motion and the steepness of the incident wave to be small - conditions that are not fulfilled in this case either. Thus, the accuracy of the model provided by the WS approximation is expected to be better than the linear theory.

For OWSC, it is well known that linear theory over-predicts the energy performance in comparison to experiment. The difference is usually attributed to viscous damping and vortex shedding. Our study shows that nonlinear effects due to large amplitude body motion are responsible for a large share of the power reduction. Further work is required to clarify which mechanisms are the most important (vortex shedding or nonlinear effects due to large body motion).

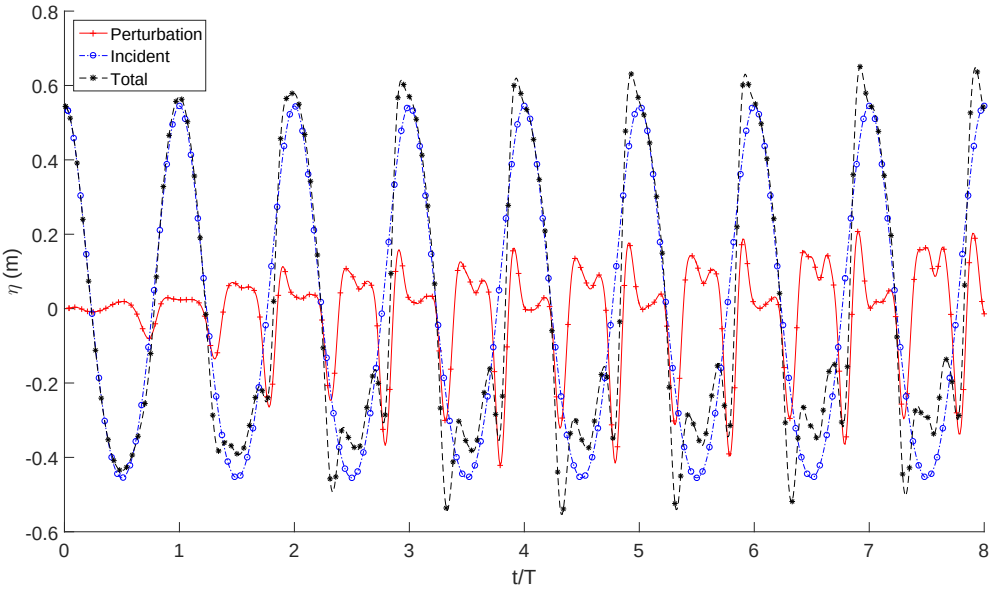

Figure 21: Incident and perturbation wave elevation, above the SOWSC, for $\omega = 0.8$ rad/s, $A_\omega = 0.5$ m

6. CONCLUSIONS

A new flow solver based on the WS method has been developed to model the particular characteristics of various WECs. Details of the implementation of the method are reported in this paper. For studying free moving bodies, the equations of motion have been integrated into the BVP of the time derivative of the velocity potential, following the Implicit Condition method. An alternative expression, developed in [29], was used for the body condition of this BVP, unifying the two expressions given by Cointe [28] and Tanizawa [27]. The WS code has been verified for a Submerged Heaving Wave Energy Converter (SHWEC) and a Submerged Oscillating Wave Surge Converter (SOWSC) by comparing numerical simulations in linear conditions against results from linear theory. Time traces of the motion response and hydrodynamic forces have shown excellent agreement for different excitation frequencies, with or without PTO damping. The motion and power responses for a wide range of frequencies have then been studied, using a Fourier analysis. The differences between the two models have been shown to be smaller than 1% in both cases.

Moving to nonlinear conditions, with large body motions and large incident wave steepness, significant differences are observed between linear theory and the WS method. For large body motions, linear theory tends to overestimate the motion and power responses, up to 200% for the SOWSC. In contrast, linear theory underestimates the response in the presence of nonlinearities related to steep incident waves. In comparisons of linear theory to nonlinear models, overestimation is more commonly cited than underestimation. In the former case, the range of frequencies over which the overestimation is

observed is close to the operating frequencies of the WEC, for which the power response is maximum. These differences show that body nonlinearities may have a significant impact on the performance of WEC. Thus, in Wave to Wire models of WECs, it may be beneficial to use the WS method or at least the body exact theory method, rather than linear theory alone. For the two nonlinear cases, the cpu time for the WS code was two orders of magnitude greater than the real time simulated ($\frac{t_{CPU}(WS)}{T} \simeq 800$), with $T = 6.3s$ and $3.14s$ respectively. The WS code can still yield the RAO for a set of 70 frequencies in a reasonable cpu time. Of course, computational time is greatly reduced with linear potential theory. With the open source linear BEM code, Nemoh, it takes a few minutes to calculate the entire database of first-order coefficients for a typical mesh size of a few hundred panels, and less than a second to simulate the response for one wave period in the time domain. The computational time for the CN_WSC was also compared to that of a fully nonlinear numerical wave tank, in [26]. It was found that the CN_WSC is roughly one order of magnitude faster than the fully nonlinear numerical wave tank.

It has also been shown that the assumptions of the WS method should be verified *a posteriori*. Certainly, large amplitude motion may lead to large perturbations. However, although the WS method may not be valid from time to time due to the local deformation of the incident wave, its results are still expected to be more realistic in nonlinear conditions when compared with results from linear theory. Nevertheless, complementary studies comparing these results with fully nonlinear solvers or experiments may be required to assess the validity of the CN_WSC. Dissipation due to viscosity and turbulent flows are not modelled in potential flow theory. These phenomena could have a significant impact on the performance of WECs with large amplitude motion, particularly OCN_WSCs [42]. It is thus important to compare the results of the numerical models with experiments, in order to quantify the main sources of performance reduction: nonlinearities related to large body motion, or dissipation due to viscous effects.

In this work, only submerged WECs were considered. Future work will consider floating bodies. This will require development of methods for tracking and updating the waterline and automatic remeshing of the free surface. For considering irregular waves, it may be interesting to couple the CN_WSC with a High Order Spectral (HOS) wave propagation model [32]. Coupling with a multi-body dynamic algorithm may also be required to deal with WECs composed of multiple bodies with complex kinematic relationships. An extension to fully nonlinear theory is also possible, exploiting the past experience of the laboratory in this domain [13, 23, 16, 24]. Finally, the CN_WSC has not yet been parallelized, which has the potential to greatly reduce the computational time.

7. ACKNOWLEDGMENT

The authors would like to thank the French ANR (Agence Nationale de la Recherche) for their financial support of this work as part of the project ANR11-MONU-018-01 MONACOREV.

BIBLIOGRAPHY

[1] A. Falcão, Wave energy utilization: A review of the technologies, Renewable and Sustainable Energy Reviews 14 (3) (2010) 899–918.

[2] P. Ricci, J. Saulnier, F. Antonio, M. Pontes, Time domain models and wave energy converters performance assessment, in: ASME 27th International Conference on Offshore Mechanics and Artic Engineering, Estoril, Portugal, 699—-708, 2008.

[3] A. McCabe, An appraisal of a range of fluid modelling software, Supergen Marine Workpackage 2 (October) (2004) 84.

[4] M. Folley, T. W. T. Whittaker, J. V. Hoff, The design of small seabed-mounted bottom-hinged wave energy converters, in: 7th European Wave and Tidal Energy Conference, Porto, Portugal, 10, 2007.

[5] A. Day, A. Babarit, A. Fontaine, Y.-P. He, M. Kraskowski, M. Murai, I. Penesis, F. Salvatore, H.-K. Shin, Hydrodynamic modelling of marine renewable energy devices: A state of the art review, Ocean Engineering 108 (2015) 46 – 69.

[6] J. Falnes, Ocean Waves and Oscillating Systems : Linear interaction including wave energy extraction., Cambridge University Press, 2002.

[7] M. Durand, A. Babarit, B. Pettinotti, O. Quillard, J. Toularastel, A. H. Clément, Experimental validation of the performances of the SEAREV Wave Energy Converter with real time latching control, in: 7th European Wave and Tidal Energy Conference, Porto, Portugal, 8, 2007.

[8] A. Babarit, H. Mouslim, A. H. Clément, P. Laporte-weywada, On the Numerical Modelling of the Non Linear Behaviour of a Wave Energy Converter, in: ASME 2009 28th International Conference on Ocean, Offshore and Arctic Engineering, American Society of Mechanical Engineers, Honolulu, Hawaii, USA, 1045–1053, 2009.

[9] J. S. Pawlowski, A Non-linear Theory of Ship Motion in Waves, Society of Naval Architects and marine Engineers 99 (1991) 319–352.

[10] Carnegie Wave Energy, CETO Commercial Scale Unit Overview, URL `Availableat:http://www.carnegiewave.com/index.php`, 2013.

[11] AW-Energy, WaveRoller concept, plug into wave energy, URL `http://aw-energy.com/about-waveroller/waveroller-concept`, 2015.

[12] M. S. Longuet-Higgins, E. D. Cokelet, The Deformation of Steep Surface Waves on Water. I. A Numerical Method of Computation, Proceedings of the Royal Society of London. A. Mathematical and Physical Sciences 350 (1660) (1976) 1 –26.

[13] P. Ferrant, Three-dimensional unsteady wave-body interactions by a Rankine boundary element method, Ship Technology Research 40 (4) (1993) 165–175.

[14] S. Grilli, P. Guyenne, F. Dias, A fully non-linear model for three-dimensional overturning waves over an arbitrary bottom, International Journal for Numerical Methods in Fluids 35 (2001) 829 – 867.

[15] W. Koo, M.-H. Kim, Freely floating-body simulation by a 2D fully nonlinear numerical wave tank, Ocean Engineering 31 (16) (2004) 2011–2046.

[16] P. Ferrant, Fully Non-Linear Interactions of Long-Crested Wave Packets with a Three -Dimensional Body, in: 22nd ONR Symposium on Naval Hydrodynamics, 403–415, 1998.

[17] K. Tanizawa, The state of the art on numerical wave tank, in: 4th Osaka colloquium on seakeeping performance ships, 95–114, 2000.

[18] Y.-L. Shao, O. M. Faltinsen, A harmonic polynomial cell (HPC) method for 3D Laplace equation with application in marine hydrodynamics, Journal of Computational Physics 274 (2014) 312–332.

[19] C. Fochesato, F. Dias, A fast method for nonlinear three-dimensional free-surface waves, Proceedings of the Royal Society A: Mathematical, Physical and Engineering Sciences 462 (2073) (2006) 2715–2735.

[20] Y. Huang, Nonlinear ship motions by a Rankine panel method, Ph.D. thesis, Massachussets Institute of Technology, 1997.

[21] W. Lin, M. Meinhold, N. Salvesen, D. K. P. Yue, Large-amplitude ship motions and wave loads for ship design, in: 20th Symposium on Naval Hydrodynamics, California, USA, 10, 1994.

[22] K.-H. Kim, Y. Kim, Time-Domain Analysis of Nonlinear Ship Motion Responses Based on Weak-scatterer Hypothesis, in: 19th International Offshore and Polar Engineering Conference, vol. 1, Osaka, Japan, 583–589, 2009.

[23] P. Ferrant, Radiation and Diffraction of Nonlinear Waves in Three Dimensions, in: the BOSS'94 Conference, Massachussets Institute of Technology, 1994.

[24] B. Büchmann, P. Ferrant, J. Skourup, Runup on a Body in Waves and Current. Fully Non-Linear and Finite Order Calculations, Applied Ocean Research 22 (6) (2000) 349–360.

[25] P. Ferrant, Analytical expressions of the influence coefficients of linear isoparametric triangular elements, personal notes, 1989.

[26] L. Letournel, J. C. Harris, P. Ferrant, G. Ducrozet, M. Benoit, E. Dombre, Comparison of fully nonlinear and weakly nonlinear potential flow solvers, in: ASME 2014 33rd International Conference on Ocean, Offshore and Arctic Engineering, American Society of Mechanical Engineers, San Francisco, California, USA, 10, 2014.

[27] K. Tanizawa, A Nonlinear Simulation Method of 3-D Body Motions in Waves (1st Report), Journal of the Society of Naval Architects of Japan 1995 (178) (1995) 179–191.

[28] R. Cointe, Quelques aspects de la simulation numérique d'un canal à houle, Ph.D. thesis, École Nationale des Ponts et Chaussées, 1989.

[29] L. Letournel, G. Ducrozet, A. Babarit, P. Ferrant, Proof of the equivalence of Tanizawa–Berkvens' and Cointe–van Daalen's formulations for the time derivative of the velocity potential for non-linear potential flow solvers, Applied Ocean Research 63 (2017) 184–199.

[30] J. Wehausen, E. Laitone, Surface Waves, Springer, 1960.

[31] M. Rienecker, J. Fenton, A Fourier approximation method for steady water waves, Journal of Fluid Mechanics 104 (1981) 119–137.

[32] G. Ducrozet, F. Bonnefoy, D. Le Touzé, P. Ferrant, HOS-ocean: Open-source solver for nonlinear waves in open ocean based on High-Order Spectral method, Computer Physics Communications 203 (2016) 245–254.

[33] R. Cointe, P. Geyer, B. King, B. Molin, M. Tramoni, Nonlinear and linear motions of a rectangular barge in a perfect fluid, in: 18th Symposium on Naval Hydrodynamics, Ann Arbor, MI, USA, 85, 1990.

[34] E. F. G. van Daalen, Numerical and Theoretical Studies of Water Waves and Floating Bodies, Ph.D. thesis, University of Twente, The Netherlands, 1993.

[35] E. Guerber, Modélisation numérique des intéractions non-linéaires entre vagues et structures immergées, appliquée à la simulation de systèmes houlomoteurs, Ph.D. thesis, Unversité Paris-Est, 2011.

[36] E. Guerber, M. Benoit, S. T. Grilli, C. Buvat, A fully nonlinear implicit model for wave interactions with submerged structures in forced or free motion, Engineering Analysis with Boundary Elements 36 (7) (2012) 1151–1163, ISSN 09557997.

[37] P. Guével, Corps solide animé d'un mouvement quelconque dans un fluide illimité, Lecture Notes, École Centrale de Nantes, 1976.

[38] L. Letournel, Développement d'un outil de simulation numérique basé sur l'approche Weak-Scatterer pour l'étude des systèmes houlomoteurs en grands mouvements, Ph.D. thesis, École Centrale de Nantes, 2015.

[39] Y. Saad, M. H. Schultz, GMRES: A generalized minimal residual algorithm for solving nonsymmetric linear systems, SIAM Journal on scientific and statistical computing 7 (3) (1986) 856–869.

[40] P. Ferrant, K. Pelletier, Second order wave diffraction patterns about complex offshore structures, in: The Tenth International Offshore and Polar Engineering Conference, International Society of Offshore and Polar Engineers, 2000.

[41] A. Babarit, G. Delhommeau, Theoretical and numerical aspects of the open source BEM solver NEMOH, in: 11th European Wave and Tidal Energy Conference (EWTEC2015), Nantes, France, 10, 2015.

[42] M. A. Bhinder, A. Babarit, L. Gentaz, P. Ferrant, et al., Effect of viscous forces on the performance of a surging wave energy converter, in: 22nd International Offshore and Polar Engineering Conference, International Society of Offshore and Polar Engineers, 5, 2012.

[43] M. Bonnet, Équations intégrales et éléments frontières, CNRS Editions / Eyrolles, 1995.

AppendixA. Development of the integral equations with a linear discretization

The two integral equations used for the solution of the boundary value problem are:

$$\iint_S \frac{\partial \phi(\mathbf{x}_l)}{\partial n} G(\mathbf{x}, \mathbf{x}_l) dS \tag{A.1}$$

$$\iint_S \phi(\mathbf{x}_l) \frac{\partial G(\mathbf{x}, \mathbf{x}_l)}{\partial n} dS \tag{A.2}$$

The integrals can be evaluated by summing over each element of the fluid domain boundary. The discretization, i.e. the variation of the quantities ϕ and $\frac{\partial \phi}{\partial n}$ across one element, is linear. Analytical expressions for the constant panel approximation have been described previously by Guevel [37]. The extension of these analytic expressions to a piecewise linear approximation was described by Ferrant [25], and implemented in [13, 23]. In addition to the improvement in accuracy afforded by this piecewise linear method, the scheme is especially efficient, in terms of the ratio between the number of unknowns and the number of panels (typically close to 1:2). Higher order discretizations can provide even greater accuracy, but rely on numerical solution, whose associated computational times are higher than with the analytical calculations. The linear discretization was thus chosen as a good trade-off between accuracy and computational time.

AppendixA.1. Discretization

The discretization is based on triangular elements, with quantities varying linearly across the elements.

AppendixA.1.1. Parametric system

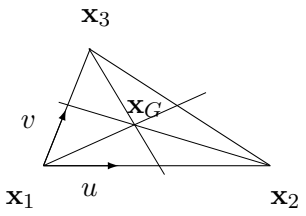

Figure A.22: Parameters

The following parameters are defined on each element, as seen in fig A.22

$$\mathbf{x} = \mathbf{x}_1 + u \times \mathbf{x_1 x_2} + v \times \mathbf{x_1 x_3} \tag{A.3}$$

This discretization is isoparametric : the parametric function f describes the geometry and the variations in the quantities.

$$\begin{aligned} f(\mathbf{x}) &= f(\mathbf{x}_1) + u \times (f(\mathbf{x}_2) - f(\mathbf{x}_1)) + v \times (f(\mathbf{x}_3) - f(\mathbf{x}_1)) \\ &= (1 - u - v) \times f(\mathbf{x}_1) + u \times f(\mathbf{x}_2) + v \times f(\mathbf{x}_3) \end{aligned} \tag{A.4}$$

The centre of gravity of the element is located at $(u, v) = \left(\frac{1}{3}, \frac{1}{3}\right)$, leading to:

$$\begin{cases} \mathbf{x}_G & = & \dfrac{\mathbf{x}_1}{3} + \dfrac{\mathbf{x}_2}{3} + \dfrac{\mathbf{x}_3}{3} \\ f(\mathbf{x}_G) & = & \dfrac{1}{3} f(\mathbf{x}_1) + \dfrac{1}{3} f(\mathbf{x}_2) + \dfrac{1}{3} f(\mathbf{x}_3) \end{cases} \tag{A.5}$$

Since the function f varies linearly, its local derivatives are constant on the element. It can then be expressed, using the surface gradient $\nabla_s f$, as:

$$f(\mathbf{x}) = f(\mathbf{x}_G) + \nabla_s f \cdot \mathbf{x_G x} \tag{A.6}$$

The surface gradient has a zero normal derivative, in contrast to the total gradient.

$$\nabla_s f = \nabla f - (\nabla f \cdot \mathbf{n})\, \mathbf{n} \tag{A.7}$$

AppendixA.1.2. Gradient expression

The expression for the surface gradient requires the local derivatives of the function f, along u and v:

$$\begin{cases} f_{,u}(\mathbf{x}) & = & \dfrac{\partial f(\mathbf{x})}{\partial u} = f(\mathbf{x}_2) - f(\mathbf{x}_1) \\ f_{,v}(\mathbf{x}) & = & \dfrac{\partial f(\mathbf{x})}{\partial v} = f(\mathbf{x}_3) - f(\mathbf{x}_1) \end{cases} \tag{A.8}$$

and the local derivatives of the parametric system:

$$\begin{cases} \mathbf{x}_{,u} = \dfrac{\partial \mathbf{x}}{\partial u} = \mathbf{x_1 x_2} \\ \mathbf{x}_{,v} = \dfrac{\partial \mathbf{x}}{\partial v} = \mathbf{x_1 x_3} \end{cases} \tag{A.9}$$

The metric tensor is then defined as:

$$\mathcal{G} = \begin{pmatrix} \| \mathbf{x_1 x_2} \|^2 & \mathbf{x_1 x_2} \cdot \mathbf{x_1 x_3} \\ \mathbf{x_1 x_2} \cdot \mathbf{x_1 x_3} & \| \mathbf{x_1 x_3} \|^2 \end{pmatrix} \tag{A.10}$$

and its inverse is:

$$g = \mathcal{G}^{-1} = \frac{1}{\Delta} \begin{pmatrix} \| \mathbf{x_1 x_3} \|^2 & -\mathbf{x_1 x_2} \cdot \mathbf{x_1 x_3} \\ -\mathbf{x_1 x_2} \cdot \mathbf{x_1 x_2} & \| \mathbf{x_1 x_2} \|^2 \end{pmatrix} \tag{A.11}$$

where $\Delta = \| \mathbf{x_1 x_2} \|^2 \times \| \mathbf{x_1 x_3} \|^2 - (\mathbf{x_1 x_2} \cdot \mathbf{x_1 x_3})^2$.

The gradient of the parametric function is then given by [43]:

$$\nabla f = \frac{\partial f}{\partial u} \times \left(g_{11} \frac{\partial \mathbf{x}}{\partial u} + g_{12} \frac{\partial \mathbf{x}}{\partial v} \right) + \frac{\partial f}{\partial v} \times \left(g_{21} \frac{\partial \mathbf{x}}{\partial u} + g_{22} \frac{\partial \mathbf{x}}{\partial v} \right) + \frac{\partial f}{\partial n} \times \mathbf{n} \tag{A.12}$$

from which it follows that the surface gradient is:

$$\begin{aligned}\nabla_s f &= \frac{f(\mathbf{x}_2)-f(\mathbf{x}_1)}{\Delta}\times\left(\parallel \mathbf{x_1x_3} \parallel^2 \times\mathbf{x_1x_2}-\mathbf{x_1x_2}\cdot\mathbf{x_1x_3}^2\right)\\ &+ \frac{f(\mathbf{x}_3)-f(\mathbf{x}_1)}{\Delta}\times\left(\parallel \mathbf{x_1x_2} \parallel^2 \times\mathbf{x_1x_3}-\mathbf{x_1x_2}^2\cdot\mathbf{x_1x_3}\right)\end{aligned} \tag{A.13}$$

This can be expressed as a function of the values of f on the nodes:

$$\nabla_s f = \overline{\overline{\Sigma}}\cdot\begin{pmatrix} f(\mathbf{x}_1)\\ f(\mathbf{x}_2)\\ f(\mathbf{x}_3)\end{pmatrix} \tag{A.14}$$

where

$$\begin{cases}\overline{\overline{\Sigma}} &= \dfrac{1}{\Delta}\times\begin{bmatrix}-(\mathbf{A}+\mathbf{B}) & \mathbf{A} & \mathbf{B}\end{bmatrix}\\ \mathbf{A} &= \parallel \mathbf{x_1x_3} \parallel^2 \times\mathbf{x_1x_2}-\mathbf{x_1x_2}\cdot\mathbf{x_1x_3}^2\\ \mathbf{B} &= \parallel \mathbf{x_1x_2} \parallel^2 \times\mathbf{x_1x_3}-\mathbf{x_1x_2}^2\cdot\mathbf{x_1x_3}\end{cases} \tag{A.15}$$

AppendixA.2. Integral equation for the normal velocity

The integral $I_\sigma(\mathbf{x},i)$ can be decomposed, for each field point $\mathbf{x}$, on each element $\mathcal{S}_i$ of the fluid domain boundary. σ refers to the single source distribution that generates the normal velocity field $\frac{\partial\phi}{\partial n}$.

$$I_\sigma(\mathbf{x},i)=\iint_{\mathcal{S}_i}\frac{\partial\phi(\mathbf{x}_l)}{\partial n}G(\mathbf{x},\mathbf{x}_l)dS \tag{A.16}$$

The linear variation of the source distribution can be written for a point $\mathbf{x}_l\in\mathcal{S}_i$ as:

$$\sigma(\mathbf{x}_l)=\sigma(\mathbf{x}_G)+\nabla_s\sigma\cdot\mathbf{x_Gx_l} \tag{A.17}$$

The center of gravity, $\mathbf{x}_G$, and the surface gradient, $\nabla_s\sigma$, are related to the element $\mathcal{S}_i$, and should also be indexed i. However, this index will be omitted in order to facilitate the legibility of the following equations.

The integral equation $I_\sigma(\mathbf{x},i)$ can then be written as:

$$\begin{aligned}I_\sigma(\mathbf{x},i) &= \sigma(\mathbf{x}_G)\iint_{\mathcal{S}_i}\frac{1}{\parallel \mathbf{xx_l} \parallel}dS+\nabla_s\sigma\cdot\iint_{\mathcal{S}_i}\frac{\mathbf{x_Gx_l}}{\parallel \mathbf{xx_l} \parallel}dS\\ &= (\sigma(\mathbf{x}_G)+\nabla_s\sigma\cdot\mathbf{x_Gx})\iint_{\mathcal{S}_i}\frac{1}{\parallel \mathbf{xx_l} \parallel}dS+\nabla_s\sigma\cdot\iint_{\mathcal{S}_i}\frac{\mathbf{xx_l}}{\parallel \mathbf{xx_l} \parallel}dS\end{aligned} \tag{A.18}$$

Using the Kelvin formula, the second double integral can be converted to a contour integral:

$$\iint_S\nabla f dS=\oint_C f\mathbf{n}_S\wedge\mathbf{dl} \tag{A.19}$$

since:

$$\frac{\mathbf{xx_l}}{\parallel \mathbf{xx_l} \parallel} = \nabla(\parallel \mathbf{xx_l} \parallel) \tag{A.20}$$

leading to:

$$I_\sigma(\mathbf{x}, i) = (\sigma(\mathbf{x}_G) + \nabla_s\sigma \cdot \mathbf{x_G x}) \iint\limits_{\mathcal{S}_i} \frac{1}{\parallel \mathbf{xx_l} \parallel} dS + \nabla_s\sigma \cdot \oint\limits_{\mathcal{C}_i} \parallel \mathbf{xx_l} \parallel \mathbf{n} \wedge \mathbf{dl} \tag{A.21}$$

By using eq A.14, it is possible to isolate values of σ on the nodes:

$$I_\sigma(\mathbf{x}, i) = \left[\left(\frac{1}{3}\bar{I} + \mathbf{x_G x} \cdot \bar{\bar{\Sigma}} \right) \iint\limits_{\mathcal{S}_i} \frac{1}{\parallel \mathbf{xx_l} \parallel} dS - \left(\oint\limits_{\mathcal{C}_i} \parallel \mathbf{xx_l} \parallel \times \mathbf{n} \wedge \mathbf{dl} \right) \cdot \bar{\bar{\Sigma}} \right] \cdot \begin{pmatrix} \sigma_1 \\ \sigma_2 \\ \sigma_3 \end{pmatrix} \tag{A.22}$$

where $\bar{I}$ is the third dimension identity matrix.

The following integrals are functions of geometrical characteristics only, dependent on $\mathbf{x}$ and $\mathcal{S}_i$:

$$S_\sigma = \iint\limits_{\mathcal{S}_i} \frac{1}{\parallel \mathbf{xx_l} \parallel} dS \quad \text{and} \quad \mathbf{I}_\sigma = \oint\limits_{\mathcal{C}_i} \parallel \mathbf{xx_l} \parallel \times \mathbf{n} \wedge \mathbf{dl}$$

AppendixA.2.1. Analytical expression for S_σ

Regular case. An analytical expression has been derived by Guevel [37], for $\mathbf{x} \notin \mathcal{S}_i$:

$$S_\sigma = \sum_{k=1}^{3} \frac{N_k^t}{2d_k} \log\left(\frac{N_k^1}{D_k^1}\right) - 2 \mid Z \mid \arctan\left(\frac{N_k^t}{D_k^t}\right) \tag{A.23}$$

Where:

$$\begin{cases} R_k &= \parallel \mathbf{x_k x} \parallel \\ d_k &= \parallel \mathbf{x_k x_{k+1}} \parallel \\ Z &= \mathbf{x_G x} \cdot \mathbf{n} \\ N_k^1 &= R_{k+1} + R_k + d_k \\ D_k^1 &= R_{k+1} + R_k - d_k \\ N_k^t &= 2\mathbf{x_k x} \cdot (\mathbf{n} \wedge \mathbf{x_k x_{k+1}}) \\ D_k^t &= (R_{k+1} + R_k)^2 - d_k^2 + 2 \mid Z \mid \times (R_{k+1} + R_k) \end{cases} \tag{A.24}$$

If $\mathbf{x} \in \mathcal{S}_i$, i.e. $\mathbf{x} = \mathbf{x}_k$ with $k = 1, 2$ or 3, a singularity occurs.

$$\mathbf{x} = \mathbf{x}_k \Rightarrow (R_k, d_k, N_k^1, D_k^1, N_k^t, D_k^t) = (0, R_{k+1}, 2 \times R_{k+1}, 0, 0, 0) \tag{A.25}$$

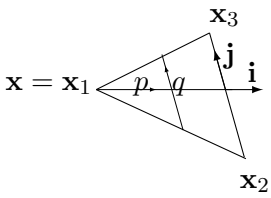

Figure A.23: Parameters for the singular case

Singular case. Suppose $\mathbf{x} = \mathbf{x}_1$. Any solution found for this particular case can be transposed for $\mathbf{x} = \mathbf{x}_2$ or $\mathbf{x} = \mathbf{x}_3$, by simply reordering the indexes.

The following parameters are defined for the element $\mathcal{S}_i$, see fig A.23:

$$\begin{cases} \mathbf{i} &= \frac{1}{2}(\mathbf{x_1 x_2} + \mathbf{x_1 x_3}) = -\mathbf{x}_1 + \frac{1}{2}(\mathbf{x}_2 + \mathbf{x}_3) \\ \mathbf{j} &= \mathbf{x_2 x_3} \\ \mathbf{h} &= \mathbf{i} \wedge \mathbf{j} \end{cases} \tag{A.26}$$

$$\mathbf{x x_l} = p\mathbf{i} + pq\mathbf{j} \qquad (p,q) \in [0,1] \times [-\frac{1}{2}, \frac{1}{2}] \tag{A.27}$$

We introduce new variables p', q' as follows:

$$\begin{cases} p &= p' \times \sqrt{\frac{\mathbf{j}^2}{\Delta}} \\ q &= \frac{\sqrt{\Delta}}{\mathbf{j}^2}\left(q' + \frac{\mathbf{i}\cdot\mathbf{j}}{\sqrt{\Delta}}\right) \end{cases} \quad \text{with} \quad \Delta = \mathbf{i}^2 \times \mathbf{j}^2 - (\mathbf{i}\cdot\mathbf{j})^2 \tag{A.28}$$

The integration limits are thus:

$$(p', q') \in \left[0, \sqrt{\frac{\Delta}{\mathbf{j}^2}}\right] \times [-a+b, a+b] \quad \text{with} \quad a = \frac{1}{2} \times \frac{\mathbf{j}^2}{\sqrt{\Delta}} \text{ and } b = \frac{(\mathbf{i}\cdot\mathbf{j})}{\sqrt{\Delta}} \tag{A.29}$$

The elementary surface dS is:

$$dS = \parallel \mathbf{h} \parallel pdpdq = \parallel \mathbf{h} \parallel p' \times \sqrt{\frac{\mathbf{j}^2}{\Delta}} \times \sqrt{\frac{\mathbf{j}^2}{\Delta}} dp' \times \frac{\sqrt{\Delta}}{\mathbf{j}^2} dq' = \frac{\parallel \mathbf{h} \parallel}{\sqrt{\Delta}} p' dp' dq' \tag{A.30}$$

It is then possible to write the square norm of $\mathbf{xx_l}$ as:

$$\begin{aligned}
\| \mathbf{xx_l} \|^2 &= (p \times \mathbf{i} + pq \times \mathbf{j})^2 = p^2 \times \mathbf{i}^2 + q^2 \times \mathbf{j}^2 + 2p^2 q \times \mathbf{i} \cdot \mathbf{j} \\
&= p^2 \times \left(\mathbf{i}^2 + q^2 \times \mathbf{j}^2 + 2q \times \mathbf{i} \cdot \mathbf{j}\right) \\
&= p'^2 \frac{\mathbf{j}^2}{\Delta} \times \left[\mathbf{i}^2 + q'^2 \times \frac{\Delta}{\mathbf{j}^4} \times \mathbf{j}^2 + \frac{(\mathbf{i} \cdot \mathbf{j})^2}{\mathbf{j}^4} \times \mathbf{j}^2 - 2q' \frac{\sqrt{\Delta} \times \mathbf{i} \cdot \mathbf{j}}{\mathbf{j}^4} \times \mathbf{j}^2 \right. \\
&\quad \left. + 2q' \frac{\Delta}{\mathbf{j}^2} - 2\frac{(\mathbf{i} \cdot \mathbf{j})^2}{\mathbf{j}^2}\right] \qquad \text{(A.31)} \\
&= p'^2 \frac{\mathbf{j}^2}{\Delta} \times \left[\mathbf{i}^2 + q'^2 \times \frac{\Delta}{\mathbf{j}^2} - \frac{(\mathbf{i} \cdot \mathbf{j})^2}{\mathbf{j}^2}\right] \\
&= p'^2 \frac{\mathbf{j}^2}{\Delta} \times \left[\frac{\mathbf{i}^2 \times \mathbf{j}^2 - (\mathbf{i} \cdot \mathbf{j})^2}{\mathbf{j}^2} + q'^2 \times \frac{\Delta}{\mathbf{j}^2}\right]
\end{aligned}$$

leading to:

$$\| \mathbf{xx_l} \|^2 = p'^2(1 + q'^2) \qquad \text{(A.32)}$$

The integral S_σ can be written as:

$$\begin{aligned}
S_\sigma &= \iint_{p' \times q'} \frac{1}{p' \times \sqrt{1 + q'^2}} \frac{\| \mathbf{h} \|}{\sqrt{\Delta}} p' dp' dq' \\
&= \frac{\| \mathbf{h} \|}{\sqrt{\Delta}} \times \sqrt{\frac{\Delta}{\mathbf{j}^2}} \times \int_{q'} \frac{1}{\sqrt{1 + q'^2}} dq' \\
&= \frac{\| \mathbf{h} \|}{\sqrt{\mathbf{j}^2}} \times \int_{q'} \frac{1}{\sqrt{1 + q'^2}} dq'
\end{aligned}$$

$$S_\sigma = \frac{\| \mathbf{h} \|}{\sqrt{\mathbf{j}^2}} \times [\text{asinh}(a + b) - \text{asinh}(-a + b)] \qquad \text{(A.33)}$$

or:

$$S_\sigma = \iint_{\mathcal{S}_i} \frac{1}{\| \mathbf{xx_l} \|} dS = \frac{\| \mathbf{h} \|}{\sqrt{\mathbf{j}^2}} \times \ln\left(\frac{a + b + \sqrt{1 + (a + b)^2}}{-a + b + \sqrt{1 + (-a + b)^2}}\right) \qquad \text{(A.34)}$$

AppendixA.2.2. Analytical expression for $\mathbf{I}_\sigma$

This integral can be evaluated on each side of the element. Consider a reference case, with a segment $[\mathbf{x}_A, \mathbf{x}_B]$, a point $\mathbf{x}_l$ on this segment and the field point $\mathbf{x}$. For this configuration:

$$\mathbf{I}_\emptyset = \int_{\mathbf{x}_A}^{\mathbf{x}_B} \| \mathbf{xx_l} \| \, dl \cdot \mathbf{s} \qquad \text{(A.35)}$$

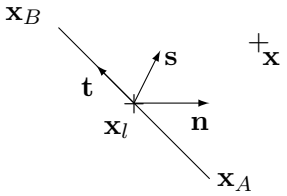

Figure A.24: Reference case

where the local base $(\mathbf{t}, \mathbf{s}, \mathbf{n})$ is defined as:

$$\begin{cases} \mathbf{t} &= \dfrac{\mathbf{x_A x_B}}{\| \mathbf{x_A x_B} \|} \\ \mathbf{s} &= \mathbf{n} \wedge \mathbf{t} = \dfrac{\mathbf{n} \wedge \mathbf{x_A x_B}}{\| \mathbf{x_A x_B} \|} \\ t &= \dfrac{\| \mathbf{x_A x_l} \|}{\| \mathbf{x_A x_B} \|}, t \in [0,1] \\ dl &= \| \mathbf{x_A x_B} \| \times dt \end{cases} \tag{A.36}$$

The square norm of $\mathbf{x x_l}$ can be written as:

$$\begin{aligned} \| \mathbf{x x_l} \|^2 &= \| \mathbf{x_A x_l} \|^2 + \| \mathbf{x_A x} \|^2 - 2\mathbf{x_A x_l} \cdot \mathbf{x_A x} \\ &= \| \mathbf{x_A x_l} \|^2 + \| \mathbf{x_A x} \|^2 - 2\frac{\| \mathbf{x_A x_l} \|}{\| \mathbf{x_A x_B} \|}\mathbf{x_A x_B} \cdot \mathbf{x_A x} \\ &= t^2 \times \| \mathbf{x_A x_B} \|^2 + \| \mathbf{x_A x} \|^2 - 2t \times \mathbf{x_A x_B} \cdot \mathbf{x_A x} \\ &= \left(t \times \| \mathbf{x_A x_B} \| - \frac{\mathbf{x_A x_B} \cdot \mathbf{x_A x}}{\| \mathbf{x_A x_B} \|} \right)^2 + \| \mathbf{x_A x} \|^2 - \left(\frac{\mathbf{x_A x_B} \cdot \mathbf{x_A x}}{\| \mathbf{x_A x_B} \|} \right)^2 \end{aligned} \tag{A.37}$$

This is equivalent to:

$$\| \mathbf{x x_l} \|^2 = K^2(1 + q^2) \tag{A.38}$$

with the following change of variables:

$$\begin{cases} K^2 &= \| \mathbf{x_A x} \|^2 - \left(\dfrac{\mathbf{x_A x_B} \cdot \mathbf{x_A x}}{\| \mathbf{x_A x_B} \|} \right)^2 \\ q &= \dfrac{1}{K} \times \left(t \times \| \mathbf{x_A x_B} \| - \dfrac{((\mathbf{x_A x_B}) \cdot (\mathbf{x_A x}))^2}{\| \mathbf{x_A x_B} \|} \right), q \in [q_0, q_1] \\ dq &= \dfrac{\| \mathbf{x_A x_B} \|}{K} \times dt \\ q_0 &= -\dfrac{\mathbf{x_A x_B} \cdot \mathbf{x_A x}}{\| \mathbf{x_A x_B} \| \times K} \\ q_1 &= \dfrac{\| \mathbf{x_A x_B} \|^2 - \mathbf{x_A x_B} \cdot \mathbf{x_A x}}{\| \mathbf{x_A x_B} \| \times K} \end{cases} \tag{A.39}$$

Introducing these variables to the integral $\mathbf{I}_\emptyset$ yields:

$$\begin{aligned}\mathbf{I}_\emptyset &= \int_{q_0}^{q_1} K^2\sqrt{1+q^2}dq\mathbf{s} \\ &= K^2 \times \int_{\text{asinh}(q_0)}^{\text{asinh}(q_1)} \sqrt{1+\sinh(x)^2} \times \cosh(x)dx \times \mathbf{s} \quad \text{with} \quad q = \sinh(x) \end{aligned} \tag{A.40}$$

(A.41)

The analytic solution for this integral is then:

$$\mathbf{I}_\emptyset = \frac{K^2}{2}\left[b - a + \frac{\sinh(2b) - \sinh(2a)}{2}\right]\mathbf{s} \tag{A.42}$$

with

$$\begin{cases} a &= \text{asinh}(q_0) \\ b &= \text{asinh}(q_1) \end{cases} \tag{A.43}$$

Singular case. While the original integral has no singularity, the solution developed here has one: if $K = 0$, the expression for q is not valid. However, $K = 0 \Longrightarrow \mathbf{x} \in (\mathbf{x}_A, \mathbf{x}_B)$, leading to the following simple solution for this case:

$$\begin{aligned}\mathbf{I}_\emptyset &= \int_{\mathbf{x}_A}^{\mathbf{x}_B} \parallel \mathbf{x}\mathbf{x_l} \parallel \times dl \cdot \mathbf{n} \wedge \mathbf{t} \\ &= \int_{\mathbf{x}_A}^{\mathbf{x}_B} \parallel \mathbf{x}\mathbf{x_A} \parallel + \parallel \mathbf{x_A}\mathbf{x_l} \parallel \times \frac{\mathbf{x_A}\mathbf{x_B} \cdot \mathbf{x_A}\mathbf{x}}{\parallel \mathbf{x_A}\mathbf{x_B} \parallel \parallel \mathbf{x_A}\mathbf{x} \parallel} dl\mathbf{s} \\ &= \parallel \mathbf{x_A}\mathbf{x_B} \parallel \parallel \mathbf{x_A}\mathbf{x} \parallel \mathbf{s} + \int_0^1 \frac{\mathbf{x_A}\mathbf{x_B} \cdot \mathbf{x_A}\mathbf{x}}{\parallel \mathbf{x_A}\mathbf{x_B} \parallel \parallel \mathbf{x_A}\mathbf{x} \parallel} t \parallel \mathbf{x_A}\mathbf{x_B} \parallel^2 dt \times \mathbf{s} \\ &= \parallel \mathbf{x_A}\mathbf{x_B} \parallel \left(\parallel \mathbf{x_A}\mathbf{x} \parallel + \frac{\mathbf{x_A}\mathbf{x_B} \cdot \mathbf{x_A}\mathbf{x}}{2 \times \parallel \mathbf{x_A}\mathbf{x} \parallel}\right)\mathbf{s}\end{aligned}$$

AppendixA.3. Integral equation for the potential

The integral $I_\mu(\mathbf{x}, i)$ can be decomposed, for each field point $\mathbf{x}$, on each element $\mathcal{S}_i$ of the fluid domain boundary. μ refers to the source doublet distribution that generates the potential field ϕ.

$$I_\mu(\mathbf{x}, i) = \iint_{\mathcal{S}_i} \phi(\mathbf{x}_l)\frac{\partial G(\mathbf{x}, \mathbf{x}_l)}{\partial n} dS \tag{A.44}$$

The singular case for this integral is inherent in the calculation of the solid angle and does not require special treatment:

$$\Omega(\mathbf{x})\phi(\mathbf{x}) = \iiint_{\mathcal{D}} \phi(\mathbf{x}_l)\Delta G(\mathbf{x}, \mathbf{x}_l) dV \tag{A.45}$$

For the regular case, a method similar to that used for the integral $I_\sigma(\mathbf{x}, i)$ is used, based on the linear expression for $\mu(\mathbf{x}_l) = \phi(\mathbf{x}_l)$ on the element $\mathcal{S}_i$:

$$\mu(\mathbf{x}_l) = \mu(\mathbf{x}_G) + \nabla_s\mu \cdot \mathbf{x_G x_l} \tag{A.46}$$

The integral $I_\mu(\mathbf{x}, i)$ can be written as:

$$I_\mu(\mathbf{x}, i) = (\mu(\mathbf{x}_G) + \nabla_s\mu \cdot \mathbf{x_G x}) \iint_{\mathcal{S}_i} \frac{\partial G(\mathbf{x}, \mathbf{x}_l)}{\partial n} dS + \nabla_s\mu \cdot \iint_{\mathcal{S}_i} \frac{\partial G(\mathbf{x}, \mathbf{x}_l)}{\partial n} \times \mathbf{x x_l} dS \tag{A.47}$$

The second integral can be converted to a contour integral by using the following vector field:

$$\mathbf{F} = -G(\mathbf{x}, \mathbf{x}_l)\,(\nabla_s\mu \wedge \mathbf{x x_l}) \tag{A.48}$$

$$\mathbf{F} = \begin{cases} \dfrac{c_\mu \times (y_l - y) - b_\mu \times (z_l - z)}{\sqrt{(x_l - x)^2 + (y_l - y)^2 + (z_l - z)^2}} \\ \dfrac{a_\mu \times (z_l - z) - c_\mu \times (x_l - x)}{\sqrt{(x_l - x)^2 + (y_l - y)^2 + (z_l - z)^2}} \\ \dfrac{b_\mu \times (x_l - x) - a_\mu \times (y_l - y)}{\sqrt{(x_l - x)^2 + (y_l - y)^2 + (z_l - z)^2}} \end{cases} \quad \text{with} \quad \nabla_s\mu = [a_\mu, b_\mu, c_\mu] \tag{A.49}$$

The normal component of the rotational of this function is the integrand of the second surface integral of Eq. A.47:

$$\begin{aligned} \mathbf{rot}(\mathbf{F}) &= [a_\mu(x_l - x) + b_\mu(y_l - y) + c_\mu(z_l - z)] \times \nabla G(\mathbf{x}, \mathbf{x}_l) \\ &\quad -2 \times G(\mathbf{x}, \mathbf{x}_l) \times \nabla_s\mu + G(\mathbf{x}, \mathbf{x}_l) \times \nabla_s\mu \\ &= (\nabla_s\mu \cdot \mathbf{x x_l})\,\nabla G(\mathbf{x}, \mathbf{x}_l) - G(\mathbf{x}, \mathbf{x}_l)\nabla_s\mu \end{aligned} \tag{A.50}$$

$$\begin{aligned} \mathbf{rot}(\mathbf{F}) \cdot \mathbf{n} &= \frac{\partial G(\mathbf{x}, \mathbf{x}_l)}{\partial n}\,(\nabla_s\mu \cdot \mathbf{x x_l}) - G(\mathbf{x}, \mathbf{x}_l)\,(\nabla_s\mu \cdot \mathbf{n}) \\ &= \frac{\partial G(\mathbf{x}, \mathbf{x}_l)}{\partial n}\,(\nabla_s\mu \cdot \mathbf{x x_l}) \end{aligned} \tag{A.51}$$

Using the fact that the normal component of the surface gradient is zero :

$$\nabla_s\mu \cdot \mathbf{n} = 0$$

Stokes' theorem can be used to transform the surface integral to a contour integral:

$$\iint_{\mathcal{S}_i} \mathbf{rot}(\mathbf{F}) \cdot \mathbf{n} dS = \oint_{\mathcal{C}_i} \mathbf{F} \cdot \mathbf{dl} \tag{A.52}$$

The second surface integral of Eq. A.47 thus becomes:

$$\begin{aligned}\iint_{\mathcal{S}_i} \frac{\partial G(\mathbf{x},\mathbf{x}_l)}{\partial n}\left(\nabla_s\mu\cdot\mathbf{xx_l}\right)dS &= \oint_{\mathcal{C}_i} -\frac{1}{\parallel \mathbf{xx_l} \parallel}\left(\nabla_s\mu\wedge\mathbf{xx_l}\right)\cdot\mathbf{dl} \\ &= -\nabla_s\mu\times\oint_{\mathcal{C}_i}\frac{\mathbf{xx_l}}{\parallel \mathbf{xx_l} \parallel}\wedge\mathbf{dl} \end{aligned} \tag{A.53}$$

The integral $I_\mu(\mathbf{x},i)$ can then be written as:

$$I_\mu(\mathbf{x},i) = \left(\mu(\mathbf{x}_G)+\nabla_s\mu\cdot\mathbf{x_G x}\right)\iint_{\mathcal{S}_i}\frac{\partial G(\mathbf{x},\mathbf{x}_l)}{\partial n}dS - \nabla_s\mu\cdot\oint_{\mathcal{C}_i}\frac{\mathbf{xx_l}}{\parallel \mathbf{x}_A-\mathbf{x} \parallel}\wedge\mathbf{dl} \tag{A.54}$$

Using Eq. A.14, it is possible to isolate values of μ on the nodes:

$$I_\mu(\mathbf{x},i) = \left[\left(\frac{\bar{I}}{3}+\mathbf{x_G x}\cdot\overline{\overline{\Sigma}}\right)\times\iint_{\mathcal{S}_i}\frac{\partial G(\mathbf{x},\mathbf{x}_l)}{\partial n}dS - \left(\oint_{\mathcal{C}_i}\frac{\mathbf{xx_l}}{\parallel \mathbf{x}_A-\mathbf{x} \parallel}\wedge\mathbf{dl}\right)\cdot\overline{\overline{\Sigma}}\right]\cdot\begin{pmatrix}\mu_1\\ \mu_2\\ \mu_3\end{pmatrix} \tag{A.55}$$

The following integrals are functions of geometrical characteristics only, dependent of $\mathbf{x}$ and $\mathcal{S}_i$:

$$S_\mu = \iint_{\mathcal{S}_i}\frac{\partial G(\mathbf{x},\mathbf{x}_l)}{\partial n}dS_P \quad \text{and} \quad \mathbf{I}_\mu = \oint_{\mathcal{C}_i}\frac{\mathbf{xx_l}}{\parallel \mathbf{xx_l} \parallel}\wedge\mathbf{dl}$$

AppendixA.3.1. Analytical expression for S_μ

The following analytical solution for the integral S_μ was provided by Guevel [37]:

$$S_\mu = 2\times\text{sign}(Z)\sum_{k=1}^{3}\arctan\left(\frac{N_k^t}{D_k^t}\right) \tag{A.56}$$

$$\begin{cases} R_k &= \parallel \mathbf{x_k x} \parallel \\ d_k &= \parallel \mathbf{x_k x_{k+1}} \parallel \\ Z &= \mathbf{x_G x}\cdot\mathbf{n} \\ N_k^t &= 2\mathbf{x_k x}\cdot(\mathbf{n}\wedge\mathbf{x_k x_{k+1}}) \\ D_k^t &= (R_{k+1}+R_k)^2 - d_k^2 + 2\mid Z\mid\times(R_{k+1}+R_k) \end{cases} \tag{A.57}$$

AppendixA.3.2. Analytical expression for $\mathbf{I}_\mu$

The integral $\mathbf{I}_\mu$ can be evaluated on either side of the element $\mathcal{S}_i$. Consider a reference case: a segment $[\mathbf{x}_A,\mathbf{x}_B]$, a point $\mathbf{x}_l$ on this segment, and the field point $\mathbf{x}$, see fig. A.25.

For this configuration:

$$\begin{aligned} I_{\emptyset} &= \int_{\mathbf{x}_A}^{\mathbf{x}_B} \frac{\mathbf{x}\mathbf{x_l}}{\| \mathbf{x}\mathbf{x_l} \|} \wedge \mathbf{dl} \\ &= \mathbf{x}\mathbf{x_A} \wedge \int_{\mathbf{x}_A}^{\mathbf{x}_B} \frac{1}{\| \mathbf{x}\mathbf{x_l} \|} \mathbf{dl} + \int_{\mathbf{x}_A}^{\mathbf{x}_B} \frac{\cancel{\mathbf{x_A}\mathbf{x_l} \wedge \mathbf{dl}}}{\| \mathbf{x}\mathbf{x_l} \|} \end{aligned} \tag{A.58}$$

Using the same parameters and variables as for integral $\mathbf{I}_\sigma$, we arrive at a simple expression for $\| \mathbf{x}\mathbf{x_l} \|$.

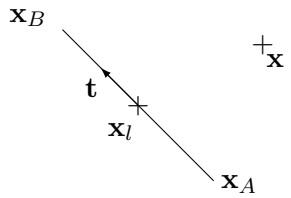

Figure A.25: Reference case

$$\begin{cases} \mathbf{t} &= \dfrac{\mathbf{x_A}\mathbf{x_B}}{\| \mathbf{x_A}\mathbf{x_B} \|} \\ t &= \dfrac{\| \mathbf{x_A}\mathbf{x_l} \|}{\| \mathbf{x_A}\mathbf{x_B} \|}, t \in [0,1] \\ dl &= \| \mathbf{x_A}\mathbf{x_B} \| \, dt \end{cases} \tag{A.59}$$

$$\| \mathbf{x}\mathbf{x_l} \|^2 = K^2(1+q^2) \tag{A.60}$$

where

$$\begin{cases} K^2 &= \| \mathbf{x_A}\mathbf{x} \|^2 - \left(\dfrac{\mathbf{x_A}\mathbf{x_B} \cdot \mathbf{x_A}\mathbf{x}}{\| \mathbf{x_A}\mathbf{x_B} \|} \right)^2 \geq 0 \\ q &= \dfrac{1}{K} \times \left(t \times \| \mathbf{x_A}\mathbf{x_B} \| - \dfrac{\mathbf{x_A}\mathbf{x_B} \cdot \mathbf{x_A}\mathbf{x}}{\| \mathbf{x_A}\mathbf{x_B} \|} \right), q \in [q_0, q_1] \\ dq &= \dfrac{\| \mathbf{x_A}\mathbf{x_B} \|}{K} \times dt \\ q_0 &= -\dfrac{\mathbf{x_A}\mathbf{x_B} \cdot \mathbf{x_A}\mathbf{x}}{\| \mathbf{x_A}\mathbf{x_B} \| \times K} \\ q_1 &= \dfrac{\| \mathbf{x_A}\mathbf{x_B} \|^2 - \mathbf{x_A}\mathbf{x_B} \cdot \mathbf{x_A}\mathbf{x}}{\| \mathbf{x_A}\mathbf{x_B} \| \times K} \end{cases} \tag{A.61}$$

If $K^2 > 0$, the integral $I_\emptyset$ can be written as:

$$\begin{aligned} \mathbf{I}_\emptyset &= -K \times \frac{\mathbf{x}\mathbf{x_A} \wedge \mathbf{x_A}\mathbf{x_B}}{\parallel \mathbf{x_A}\mathbf{x_B} \parallel} \int_{q_0}^{q_1} \frac{1}{K \times \sqrt{(1+q^2)}} \times dq \\ &= -\frac{\mathbf{x}\mathbf{x_A} \wedge \mathbf{x_A}\mathbf{x_B}}{\parallel \mathbf{x_A}\mathbf{x_B} \parallel} [\mathrm{asinh}(q_1) - \mathrm{asinh}(q_0)] \end{aligned} \tag{A.62}$$

or:

$$\mathbf{I}_\emptyset = -\frac{\mathbf{x}\mathbf{x_A} \wedge \mathbf{x_A}\mathbf{x_B}}{\parallel \mathbf{x_A}\mathbf{x_B} \parallel} \ln \left(\frac{q_1 + \sqrt{1+q_1^2}}{q_0 + \sqrt{1+q_0^2}} \right) \tag{A.63}$$

A singularity occurs for $K = 0$, which means $M \in (\mathbf{x}_A, \mathbf{x}_B)$. In this particular case, it can be shown that the integral is equal to zero, since $(\mathbf{x}\mathbf{x_l}) \wedge \mathbf{dl} = \mathbf{0}$.